Nanoscale space weathering features in mature lunar soil revealed by TEM and APT

Citation for the original published paper (version of record):
Greer, J., Kling, A., Daly, L. et al (2026). Nanoscale space weathering features in mature lunar soil revealed by TEM and APT. Meteoritics and Planetary Science, 61(8): 2048-2072.
http://dx.doi.org/10.1111/maps.70196

The Meteoritical Society

Meteoritics & Planetary Science 61, Nr 8, 2048–2072 (2026)
doi: 10.1111/maps.70196

Nanoscale space weathering features in mature lunar soil revealed by TEM and APT

Jennika GREER[1,2], Alexander M. KLING[3], Luke DALY[4,5,6], Dieter ISHEIM[7,8], David N. SEIDMAN[7,8], Michelle S. THOMPSON[3], and Philipp R. HECK[2,9]*

[1]Division of Microstructure Physics, Chalmers University of Technology, Göteborg, Sweden
[2]Robert A. Pritzker Center for Meteoritics and Polar Studies, Negaunee Integrative Research Center, Field Museum of Natural History, Chicago, Illinois, USA
[3]Department of Earth, Atmospheric, and Planetary Sciences, Purdue University, West Lafayette, Indiana, USA
[4]School of Geographical & Earth Sciences, University of Glasgow, Glasgow, UK
[5]Australian Centre for Microscopy and Microanalysis, The University of Sydney, Sydney, New South Wales, Australia
[6]Department of Materials, University of Oxford, Oxford, UK
[7]Department of Materials Science and Engineering, Northwestern University, Evanston, Illinois, USA
[8]Northwestern University Center for Atom Probe Tomography, Northwestern University, Evanston, Illinois, USA
[9]Department of the Geophysical Sciences, University of Chicago, Chicago, Illinois, USA

***Correspondence**
Philipp R. Heck, Robert A. Pritzker Center for Meteoritics and Polar Studies, Negaunee Integrative Research Center, Field Museum of Natural History, Chicago, IL 60605-2496, USA.
Email: prheck@fieldmuseum.org

(Received 16 February 2026; revision accepted 12 June 2026)

Abstract–Space weathering significantly alters the optical, chemical, and structural properties of lunar regolith at micro- and nanoscales; yet detailed nanoscale variability within individual soils remains underexplored. Here we apply transmission electron microscopy (TEM) and atom probe tomography to four mineral grains (olivine, ilmenite, and two agglutinitic grains) from mature Apollo 17 soil 79221, characterizing solar wind-induced damage, vesiculation, nanophase Fe formation, and volatile retention with nanometer resolution. Our analyses reveal pronounced heterogeneity in vesicle morphology, nanophase Fe abundance, and volatile content that varies with mineralogy and exposure history. Oxygen depletion near grain surfaces indicates sputtering effects. Beyond confirming nanoscale heterogeneity, our coordinated analyses resolve, by APT, the Fe-depleted halos around $npFe^0$ in mature ilmenite that we previously documented with the same technique in submature Apollo 17 ilmenite. We identify impact-melt quench textures that contribute non-weathering $npFe^0$ to agglutinitic grains, and find a thick damage rim with few $npFe^0$ in Mg-rich olivine accumulates. TEM observations of elongated, linear vesicles aligned parallel to ilmenite blade margins within a bladed agglutinitic grain further suggest crystallographic rather than directional control of vesicles in ilmenite inclusions. We also establish that vesicles distort APT reconstructions and degas during field evaporation, complicating quantitative inventories of $npFe^0$ and volatiles in space-weathered grains.

INTRODUCTION

Space weathering refers to the physical and chemical alteration of materials at the surfaces of airless bodies like the Moon, and is an ongoing process that has shaped the lunar surface throughout its history. This alteration can drastically change the reflectance spectral characteristics of these bodies, as observed by remote sensing via ground-based telescopes or spacecraft, compared to laboratory analysis of unweathered material (e.g., Chapman, 1996; Hapke, 2001; Keller et al., 1998; Pieters & Noble, 2016). Microstructural and chemical features produced by space weathering accumulate in surface regolith and drive the attenuation of absorption bands, reddening (increasing reflectance with increasing wavelength), and darkening (reduction in reflectance) of spectra in the visible to near-infrared wavelengths. Spectroscopic studies of the Moon are extremely useful for generating compositional data that can be used to understand its present global composition and history (Denevi et al., 2023). However, space weathering-induced spectral changes complicate the interpretation of surface composition and, consequently, our understanding of lunar history (Pieters & Noble, 2016). Therefore, it is critical to understand how lunar materials change when exposed to space weathering and to account for these processes. Notably, the chemical and structural effects of space weathering on lunar materials generally manifest at the micro- and nanoscale, necessitating nanoscale analyses.

Space weathering is driven by two primary processes: irradiation with energetic particles, from the solar wind and solar particle events (e.g., coronal mass ejections and flares), and micrometeorite impacts. With the exception of permanently shadowed craters, the lunar surface is exposed to an environment that includes the solar wind (Wurz et al., 2022), a stream of charged particles that interacts with the surface of grains to produce the variety of secondary products that we see in our samples. The solar wind is predominantly comprised of H^+ and He^+ ions with 90% of particles in the energy range of $\sim$0.5–2.5 keV amu^{-1} (Gosling, 2014). Solar wind ions penetrate the upper $\sim$100 nm of grains, sputtering atoms, generating a defect-rich, nanocrystalline to amorphous rim, producing vesicles (bubbles within the rim that can be filled with solar wind-derived species) and nanophase Fe particles (npFe) which are nanoscale particles, predominantly spherical and comprised primarily of metallic Fe^0 (Davoisne et al., 2008; Dukes et al., 1999; Kuhlman et al., 2015). The formation of npFe through H^+ irradiation only occurs at elevated temperatures ($\sim$90°C) within Fe-rich minerals (Zhang et al., 2025). The temperature dependence of npFe production rates implies a latitude dependence and accounts for the observed differences among samples from the various Apollo and Chang'e landing sites, which span from the near-equatorial Apollo 11 site to the high-latitude (>±40°) CE-5 and CE-6 collection areas (Kling et al., 2025). The solar energetic particles responsible for solar flare tracks can have energies up to 100 MeV amu^{-1} (Crozaz, 1980), and while not a major contributor to the near surface features in the grains analyzed here, high energy (1 GeV) galactic cosmic rays can also affect the regolith to a depth of $\sim$1–2 m (Leya & Masarik, 2009; Wurz et al., 2022).

In addition to energetic ions, the surface of the Moon is also bombarded with interplanetary dust particles (IDPs) and micrometeorites estimated at a total of $\sim 10^6$ kg year^{-1} of objects 10 nm to 1 mm in diameter (Grün et al., 2011), which also alters the lunar regolith. The microstructural and chemical characteristics of micrometeorite impacts include agglutinates, which are welded aggregates of grain fragments and melt (Housley et al., 1973), as well as melt and vapor layers deposited onto grain surfaces (Hapke, 2001; Keller & McKay, 1993, 1997). These melt layers, composed of glassy splashes that are compositionally distinct from the underlying grain, can range from small, micrometer-sized droplets to extended, micrometer-thick sheets that cover most of the grain. These melt features can also contain vesicles and npFe (Keller & McKay, 1997).

Soil maturity is a term that is used to describe the accumulation of space weathering products (Pieters & Noble, 2016) and is linked to the amount of npFe present in the sample (Morris, 1978). A soil's maturity is related to its exposure age, which is a quantitative measure of how long a grain has been exposed to the space weathering environment (Pieters & Noble, 2016). Despite the Moon's relatively constant distance from the Sun at 1 AU, a range of soil maturities (mature, submature, and immature) are present on its surface due to differences in exposure histories. The grain mineralogy directly influences how individual particles record their surface exposure microstructurally and chemically. For example, the total amount of npFe present in a space-weathered sample is in part a function of Fe concentration in the grain (Pieters et al., 2000); the development of defects, vesicles, and npFe can change depending on the crystallinity of the host grain (Burgess & Stroud, 2018a; Laczniak et al., 2021; Li et al., 2013; Zeng et al., 2025); and composition can affect the timing of saturation of solar flare tracks which are used to quantify the exposure age (Bibring et al., 1975; Keller et al., 2021). As npFe particles accumulate and grow in the surfaces of soil grains, their production alters the optical properties of lunar soil, darkening the reflectance spectra and reducing the strength of diagnostic absorption features (Keller et al., 1998; Noble et al., 2007; Pieters & Noble, 2016). The spectral response of a lunar soil is also influenced by its grain-size distribution: typical soils have mean grain sizes on the order of 60–80 μm, but the finest fractions, which have the largest surface-to-volume ratios, tend to dominate the bulk reflectance spectrum (McKay et al., 1991; Pieters et al., 2000; Serventi & Carli, 2017; Taylor, Pieters, Keller, Morris, & McKay, 2001). As a result, remotely measured spectra reflect an integrated signal that depends both on grain size and on the extent and type of space weathering alteration on different mineral hosts. To disentangle these effects, it is therefore important to explore the range of alteration present within different minerals of known grain size extracted from a single soil, in order to build a more complete understanding of how space weathering affects the Moon.

The nanoparticles that develop in lunar samples are typically Fe^0 (e.g., Taylor, Pieters, Keller, Morris, & McKay, 2001), but have also been observed to be present in varying states of oxidation (e.g., Burgess & Stroud, 2018b; Thompson et al., 2016) with vesicular or hollow morphologies (e.g., Cymes et al., 2024; Guo et al., 2022) or as Fe-sulfides (e.g., Noguchi et al., 2011).

Vesicles were recognized in Apollo materials both as part of redeposition rims and as isolated bubbles in solar wind-damaged rims (e.g., Burgess & Stroud, 2018a; Greer et al., 2020; Keller & McKay, 1997; Matsumoto et al., 2015; Noguchi et al., 2014) and range in size from several up to hundreds of nanometer in diameter. Vesicles in space weathering-exposed samples have been shown to host implanted solar wind H and He (e.g., Bradley et al., 2014; Burgess & Stroud, 2018a; Greer et al., 2020) and water derived from the solar wind (Bradley et al., 2014; Kling et al., 2025). Helium inside vesicles was first observed by Burgess and Stroud (2018a) using electron energy-loss spectroscopy (EELS He K-edge) with transmission electron microscopy (TEM), establishing vesicles as sealed solar wind reservoirs in lunar grains (Burgess & Stroud, 2018a). Helium has also been observed within nanophase Fe particles that contain vesicles, known as vesicular npFe (vnpFe) particles via EELS analyses (Cymes et al., 2024; Guo et al., 2024; Kling et al., 2025).

Extending this to well-provenanced nearside soils, Chang'e-5 (CE-5) ilmenite shows an ~80 nm amorphous rim subtype with nano-vesicles (<~5–10 nm) and sparse $npFe^0$, and direct observation of He with K-edge EELS in those vesicles (Guo et al., 2024). These CE-5 data confirm helium-filled vesicles in younger nearside regolith and tie vesicle occurrence to relative exposure ages of regolith grain surfaces. Prior studies show evidence for vesiculation at the microscale in blistered surface textures (e.g., Matsumoto et al., 2021; Zhu et al., 2019), but many products can only be characterized below the grain surface at the nanoscale. For the Chang'e-6 (CE-6) farside soils, TEM analyses document vesicles but also thinner amorphous layers, fewer $npFe^0$, and lower flare-track densities than nearside analogues, implying environment-dependent weathering (Lin et al., 2025). Together with recent noble-gas measurements in vesicular $npFe^0$ in lunar glasses (Cymes et al., 2024), the CE-5 results strengthen the case that vesiculation governs solar wind volatile storage, and that the structure, thickness, and composition of space-weathered rims differ systematically with local environmental conditions such as solar wind flux, micrometeoroid impact rate, and regolith thermal history (Kling et al., 2025).

Lunar soil 79221 was collected during the Apollo 17 mission at Station 9, located on the rim of Van Serg Crater in the Taurus-Littrow Valley. The sample represents the uppermost 2 cm of a 17 cm-deep trench excavated by astronaut Harrison Schmitt to investigate a striking color contrast between the dark surface regolith and underlying light-gray material (Meyer, 2009). Soil 79221 is classified as a mature mare sample ($I_s/FeO = 78$; Morris, 1978) and has previously been investigated to study space weathering on the Moon (Keller et al., 1999; Kling et al., 2025; Taylor, Pieters, Keller, Morris, McKay, et al., 2001; Thompson et al., 2016, 2017). The grains in mature soils, in both mare and feldspathic highland terrains, have accumulated significant amounts of npFe, vesicles, and glassy redeposition rims due to their relatively long exposure time scales on the lunar surface (Keller et al., 1999; Morris, 1978), although the magnitude of npFe accumulation is generally greater in mare soils owing to their higher initial Fe content (Pieters et al., 2000). The abundances of solar wind volatiles including H, C, N, He, Ne, Ar, Kr, and Xe also correlate with soil maturity (Fegley & Swindle, 1993). Additionally, mature soils also often have a higher concentration of agglutinate particles formed by micrometeorite impacts (Pieters et al., 2000).

In sampling at the nanoscale level, we observed heterogeneity in the products of space weathering that spans a wide range among different minerals and surfaces, even within the same soil sample (e.g., Greer et al., 2020; Kling et al., 2025). Soil maturity is a useful classification for soils in bulk, but the term does not capture the wide range of features that are seen in the surfaces of these individual grains at the nanoscale. In this work, we investigate this further and present a coordinated TEM and atom probe tomography (APT) study to characterize space weathered Apollo samples. Specifically, we present a variety of space weathering features from four different grains with distinct compositions, all from Apollo 17 sample Soil 79221.

METHODS

Apollo 17 soil sample 79221 was sieved to >45 μm at Purdue University using an electroformed Ni sieve (Precision Eforming) with a 45 μm mesh, in ambient air, and individual grains were transferred to a scanning electron microscope (SEM) standard (aluminum) stub covered in carbon tape. This stub was sputter-coated with Pt to prevent charging during scanning electron microscopy (SEM) analyses. Platinum coating is compatible with field-evaporation in APT. The grains

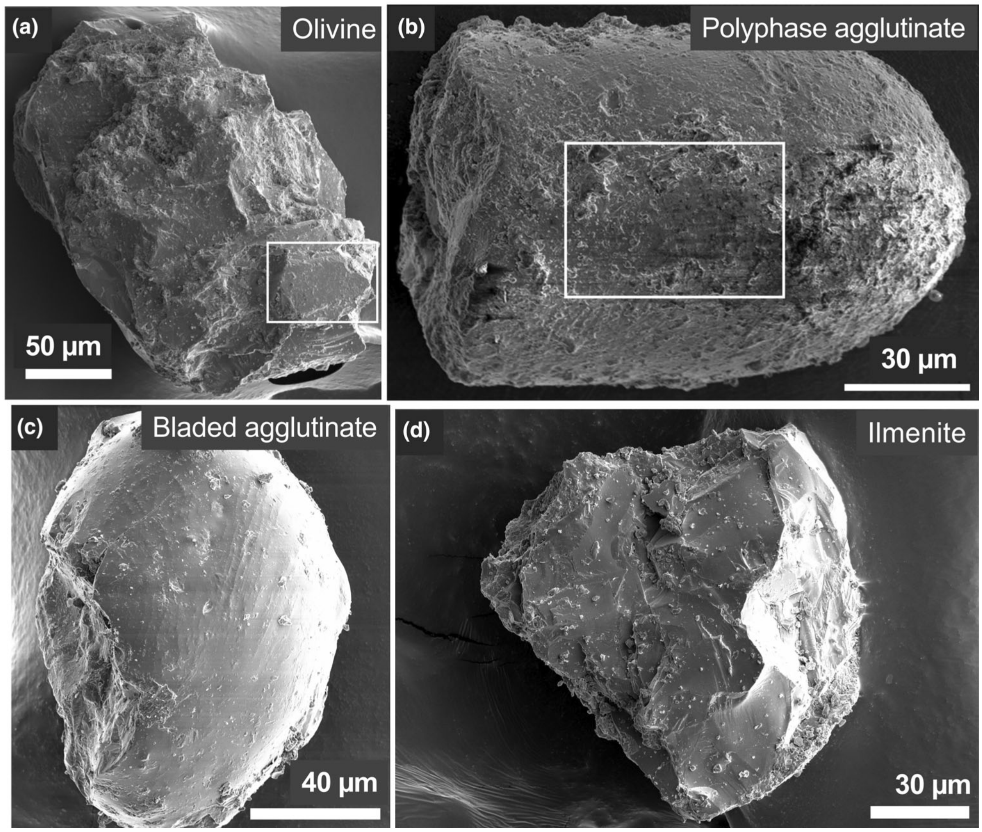

FIGURE 1. Secondary electron (SE) images of grains from Apollo 79221. (a) SE image of olivine grain. (b) SE image of polyphase agglutinitic grain. (c) SE image of bladed agglutinitic grain. (d) SE image of ilmenite grain.

were initially analyzed using secondary electron and backscatter electron imaging and using energy dispersive X-ray spectroscopy (EDS) at Purdue University with a Hitachi TM 4000 Plus benchtop SEM. Grains in the 100–200 μm range were analyzed for the identification of characteristics of space weathering including surface features such as vesicles or bubbles. Four grains were selected for further analysis, including an olivine, ilmenite, and two agglutinitic grains (Figure 1). The agglutinitic grains contained relict crystalline mineral fragments in addition to a glassy matrix and are either agglutinates or impact glass fragments.

Electron transparent lamellae (1×10 μm) from each candidate grain were focused-ion-beam (FIB) milled using the Helios G4 UX dual beam FIB-SEM at Purdue University for analysis in the TEM. These lamellae underwent initial characterization using the Tecnai T20 TEM at Purdue University to identify space-weathered rims that included solar wind-damaged rims, vesicles, and npFe particles. TEM is already a well-established technique for analyzing space weathering in lunar samples at the nanoscale (Agrell et al., 1970; Bradley et al., 2014; Burgess & Stroud, 2018a, 2018b; Christoffersen et al., 1996; Dran et al., 1970; Housley et al., 1973; Keller et al., 2021; Keller & McKay, 1993, 1997; Thompson et al., 2016). Bright-field (BF) and dark-field (DF) TEM imaging, high-resolution (HRTEM) imaging, selected-area electron diffraction (SAED), and annual dark-field (ADF) and high-angle annual dark-field (HAADF) STEM imaging, and EDS mapping were performed with the Thermo Scientific Talos 200X scanning S/TEM equipped with a Super-X silicon drift detector and the Thermo Scientific Themis Z monochromated and aberration-corrected scanning (S/TEM) equipped with a Super-X quad-silicon drift detector at Purdue University (Kling et al., 2025). Quantification of element maps and line profiles was performed in the Velox software used for EDS acquisition using the Cliff-Lorimer method. Electron energy loss spectroscopy was performed on the Themis Z equipped with a Gatan Quantum 965 EELS detector at Purdue University and the Ohio State University. EELS spectra were acquired as spectrum images in Dual-EELS mode to capture the zero-loss peak (ZLP) and the low-loss energy region (0–~50 eV). The spectra were acquired with the monochromator and an energy dispersion of 0.025 eV/ch to get an energy resolution of ~0.2 eV based on the full-width half-maximum of the ZLP. EELS spectra were processed and analyzed using the Gatan DigitalMicrograph® software and the HyperSpy open-source Python library. APT is a technique that field-evaporates atoms from the surface of a sample nanotip and uses time-of-flight mass spectrometry and a position-sensitive detector to reconstruct a digital twin of the sample in 3-D with near-atomic spatial resolution and is therefore an ideal method to elucidate the complex structure of the outermost ~100 s of nanometers of the surfaces of space weathered samples (e.g., Daly et al., 2021; Greer et al., 2020; Kling et al., 2025; Lewis et al., 2020). The combination of APT and TEM is highly complementary: APT yields 3-D chemical maps that are difficult or impossible to obtain by TEM methods alone. When used together, these approaches enable a more complete understanding of the structure–composition relationships in complex solid materials than either technique can achieve independently.

APT tips were prepared using a TESCAN LYRA3 FIB-SEM microscope at the University of Chicago. A $1 \times 10\,\mu m$ area of interest was coated with Pt to protect it from damage by the FIB, and a lamella was lifted out of each of the four target grains. These lift-outs were performed close (within 10 μm) to the location of lamellae extracted for TEM analyses in an attempt to sample the same material, but far enough to avoid beam damage from previous FIB sample preparation. Out of each lamella, 4–5 nanotips (labeled A to E) were prepared. Subsections of the lamellae were mounted on Si flat-top posts then milled to produce nanotips with apex radii of <100 nm following the methods outlined in Greer et al. (2020). Milling the tips was done with incrementally lower voltages to minimize ion beam damage and reduce Ga implantation. The majority of the nanotips were sharpened with the aim of leaving a thin layer of the Pt cap to ensure that the outermost surface of the sample was preserved, though for some nanotips the cap is missing, indicating that the outermost several nanometer of the surface may have been milled away during sample preparation. The plagioclase agglutinate more easily field-evaporated than the Pt cap protecting it, so to prevent tip failure, the cap needed to be completely milled away prior to APT analysis. Therefore, up to 20 nm may be missing from this sample.

The nanotips were analyzed at the NUCAPT facility of Northwestern University with a CAMECA LEAP 5000 XS equipped with a picosecond UV laser (wavelength = 355 nm) and run with a laser pulse energy of 40 pJ and a pulse repetition rate of 250 kHz. Samples were run at either 30 or 40 K base temperature and with a maximum detection rate of 1.5%. Tomographic reconstructions were done with CAMECA's IVAS and AP Suite 6 software. APT mass spectra and peak assignment are summarized in Figure S1 for all eight nanotips. For APT, we adopted a minimum diameter of ~1 nm for features reported as nanophase Fe inclusions, below which density fluctuations cannot be reliably distinguished from statistical noise. Reported feature sizes carry an estimated uncertainty of a factor of up to ~2, reflecting possible ion trajectory aberrations and the specific choice of the isoconcentration surface threshold used to delineate feature boundaries.

RESULTS

One to two lamellae were extracted from each grain for TEM analyses. Data are presented from one olivine section, two sections from a polyphasic agglutinitic grain, one section from an agglutinitic grain with bladed mineral inclusions, and one section from ilmenite (Figures 2–12; S1). A total of 17 nanotips were analyzed for their space weathering features, with eight providing useful data. This includes four olivine nanotips (Tips B, C, D, and E), two nanotips from the polyphase agglutinitic grain (Tips A and B), one nanotip from the bladed agglutinitic grain, and one ilmenite nanotip. The mass-to-charge state ratio spectra are presented in Figure S1.

Olivine

The olivine grain selected for analysis is ~150 μm in diameter on its longest axis and of a single compositional phase (Figure 1a). There are some fine particles adhering to the surface and there is little evidence of surface melt deposits.

TEM Analysis

Several FIB sections for TEM analysis were extracted from different regions of the grain, avoiding areas with fine particles. The selected area diffraction (SAED) pattern acquired ~2 μm deep into the grain interior, well below the solar wind-damaged rim, is indexed to forsterite (Figure 2a). Bright-field (BF) TEM imaging shows that the solar wind damaged rim is ~120 nm thick, is nanocrystalline, and overlies a grain interior that retains solar energetic particle tracks (SEP; Figure 2b). Kling et al. (2025) calculated and compared the density of these tracks in an aliquot of this sample to a calibrated SEP track production function (Keller et al., 2021) to get a surface exposure age of $\sim 4.6 \pm 0.4$ Myr. Vesicles, elongated planar defects, and chains of smaller, unconnected vesicles are observed within the solar wind-damaged rim via BF-TEM imaging (Figure 2c). Rounded vesicles ~10 nm in diameter are present in the upper ~30–50 nm of the rim. Below these larger, rounded vesicles are the elongated planar defects and chains of small vesicles that extend subparallel to the grain surface. The chains of small vesicles include sizes down to ~3 nm in diameter and the elongated planar defects span

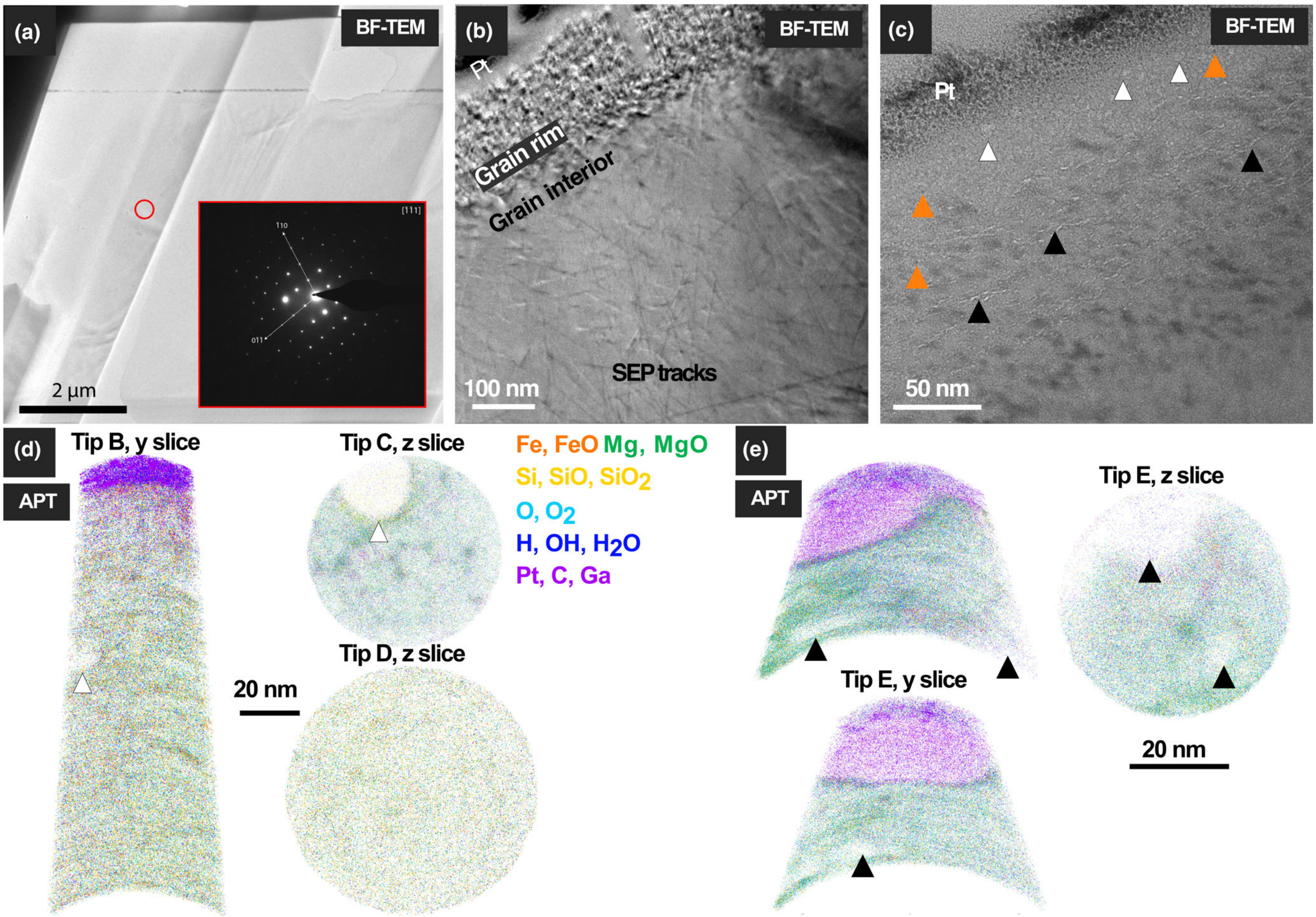

FIGURE 2. Transmission electron microscopy (TEM) images and atom probe tomography (APT) reconstructions of olivine grain from Apollo 79221. (a) Bright-field (BF-TEM) over image of the olivine FIB section. The red circle in the grain interior is where a selected area electron diffraction (SAED) pattern (inset) was collected. The SAED pattern is indexed to forsterite. (b) BF-TEM image of solar wind damaged rim of olivine overlying grain interior. The grain interior retains solar energetic particle tracks with a track density of 2×10^{11} tracks/cm^2. Using an SEP track production of $4.4 \pm 0.4 \times 10^4$ tracks/cm^2 year^{-1} (Keller et al., 2021), this track density corresponds to a surface exposure age of ~4.6 ± 0.4 Myr. (c) Higher magnification BF-TEM image of solar wind-damaged rim. The rim contains vesicles (white arrows), elongated defects (black arrows), and nanophase Fe particles (orange arrows). (d) Slices through the APT reconstructions of olivine tips B, C, and D. Each colored dot represents an individual ion, and color assignments for each ion are given in the legend. Species in purple are not intrinsic to the sample and were introduced during sample preparation. Rounded vesicles are labeled with white arrows. The thickness of each slice is between 3 and 5 nm, selected to best show features. (e) Slices in x, y, and z through olivine tip E. Some of the elongated defects are labeled with black arrows. (Color figure can be viewed at wileyonlinelibrary.com)

10–30 nm long. ~3 nm diameter nanophase Fe (npFe) particles are also present (Figure 2c). High-resolution TEM (HRTEM) imaging and fast-Fourier transform (FFT) analyses of regions throughout the rim show that while still nanocrystalline, there is a greater degree of amorphization of the rim toward the surface as revealed by the decreasing number of diffraction spots present (Figure S2). Quantitative EDS analyses of the grain interior reveal that the olivine grain is Mg-rich, with a Fo number ~93 (Figure 3a). EDS analyses of the space weathered rim show that its cation relative abundance is broadly consistent with that of the grain's interior, indicative of a solar wind-damaged rim rather than a melt- or vapor-deposited rim (Keller & McKay, 1997), and consistent with the surface morphology at the locations where the FIB lamellae were extracted. Oxygen appears to be slightly depleted in the upper ~50 nm of the grain surface, and some heterogeneity occurs in the concentration depth profiles of Mg and Si in the solar wind-damaged rim (Figure 3a).

Low-loss EELS analyses of the olivine are dominated by a bulk plasmon peak centered at ~21.5 eV in the rim and ~23 eV in the grain interior. The spectra demonstrate both a broadening of the plasmon peak and a shift in the

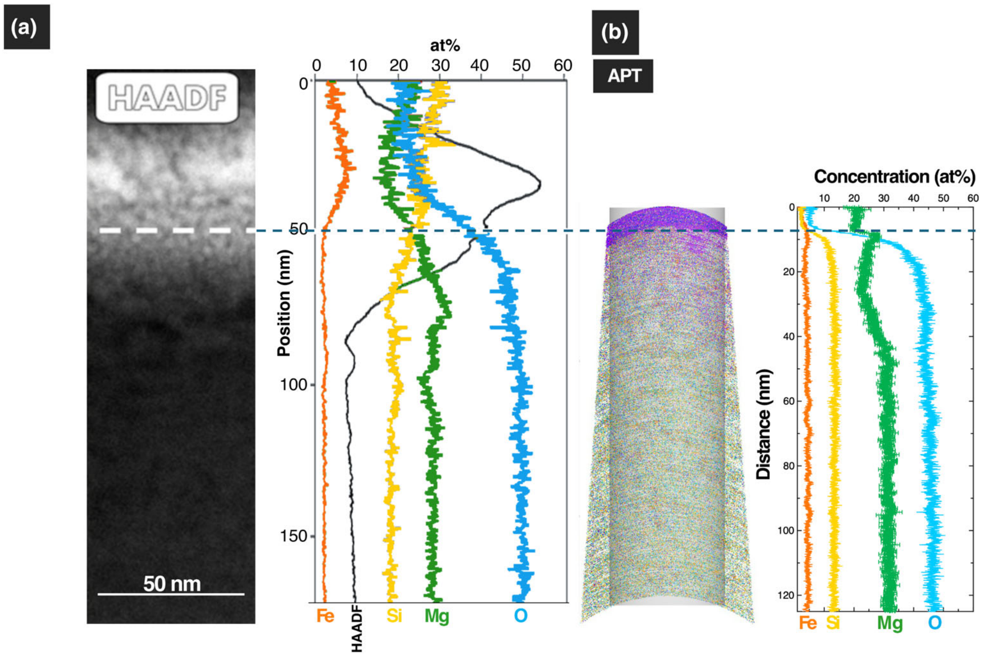

FIGURE 3. Compositional profiles through space-weathered rim of olivine. The grain surface is denoted by the dashed line. (a) TEM Dark field image and EDS profile of the olivine grains surface. (b) APT reconstruction and concentration profiles. The concentration values above the dashed line in the profiles could be influenced by redeposition during sputtering with FIB sample preparation. Nevertheless, depletion of oxygen in the rim relative to the interior, apparent in both EDS and APT profiles, likely is due to preferential sputtering from the solar wind (Loeffler et al., 2009). The small changes in enrichment and depletion of Mg and Si in the rim are similar to those observed in experimentally irradiated olivine (Laczniak et al., 2024). (Color figure can be viewed at wileyonlinelibrary.com)

plasmon peak toward lower energy loss values within the rim relative to the grain interior (Figure S3). In other investigations of similar samples, spectra from the rim and from within vesicles show the presence of the hydrogen K-edge (H-K), helium K-edge (He-K), and energy gap of water (EG), indicating the presence of H, He, and water, respectively (Kling et al., 2025). Peaks in the spectra were also identified at ~15 eV and are attributed to surface plasmons that result from the interaction of the electron beam and the specimen surface. This peak corresponds well with the predicted surface plasmon energy (ωs) of ~15.2 eV which can be calculated from the energy of the bulk plasmon ωp by the equation $\omega s = \omega p 2^{-½}$ (Rocca, 1995). A peak was also identified in olivine at ~10.5 eV which is likely due to the SiO_4^{4-} exciton (Weinberg et al., 1979) previously observed in olivine, quartz, amorphous silica, and IDPs (Bradley & Dai, 2009; Bradley et al., 2005, 2014; Erni et al., 2005). The assignment of features in the EG energy region to water is supported by the coordinated detection of H^+, OH^+, and H_2O^+ ions in APT measurements of aliquots from the same grains, reported in Kling et al. (2025).

APT Results

Olivine nanotips B, C, D, and E successfully sampled target material (Figure 2d,e). Capping materials (Pt and C) were present at the apex of Tip B, confirming that this tip captured the outermost olivine grain surface. Tip C did not preserve the outermost surface, but did contain a large void space. This tip fractured after a relatively short analytical run, likely because the void space that is present, likely a spherical vesicle ~20 nm in diameter, caused the mechanical failure of the tip. Tip D did not have a discrete layer of capping materials, but the slightly increased concentration of Pt at the top suggests that it captured the area very close to the surface of the grain. Olivine Tip E contains capping material, some of which filled in a cavity in the surface. While this could be a nanoscale irregularity on the surface, it could also be a vesicle that was exposed to the surface before sample analysis. This tip also contained a large void space (>20 nm, visible in the *z*-slice in Figure 2e) similar to the network of defects that was observed with TEM (black arrows in Figure 2c). In Tip E, there are also at least two smaller void spaces ~5 nm in diameter that appear to be vesicles (black arrows in *y* and *z* slices of Figure 2e). This tip fractured likely because the defect passed through the tip, resulting in a geometry that was not stable during field-evaporation. Tip B ran longer and most vesicles appear to be located in the first ~70 nm depth (Figure 2d).

Some nanotips had zones of decreased atom density that could be interpreted as vesicles (such as in the upper left of Tip C, Figure 2d). Other tips showed areas of increased density, which are represented as clusters of increased concentration in all elements. The void space structures can be quite complex in shape and distribution, as seen in Figure 2e. Some of the void spaces are not simply individual, isolated bubbles but instead have complicated geometries, also observed with TEM (Figure 2c). APT elemental concentration depth profiles (Figure 3b) generally agree with those from TEM-EDS, with O depleted at the surface. Fe is distributed heterogeneously and with clusters corresponding to npFe. There are several isobaric overlaps between major element species, which are assigned to a single species based on the overall isotopic pattern in the spectra relative to known isotopic abundances. The peak at 28 Da is assigned to Fe^{56++} since Si^{28} is mostly detected double charged (Si^{28++} at 14 Da). The single peak at 44 Da may include $(Fe^{56}O^{16}{}_2)^{++}$ ions but is typically assigned to $(Si^{28}O^{16})^+$. In the reconstructions, the peak at 44 Da does not exhibit the same clustering patterns as ions from other, less ambiguous Fe peaks, that is, 28 and 56 Da. The simplification of assigning the peak at 44 to $(Si^{28}O^{16})^+$ may, however, result in an underestimation of the Fe concentration in the Si-rich mineral matrix.

Polyphase Agglutinitic Grain

SEM imaging of the agglutinitic grain shows that it has a bullet-like shape, flat on one end and rounded on the other. This grain exhibits some surface melt deposits (Figure 1b).

TEM Analyses

TEM analyses of the agglutinitic grain (Figure 4) reveal embedded crystalline mineral fragments and inclusions within a glassy matrix. EDS analyses of the glassy material of the agglutinitic grain indicate it is predominantly composed of Si, Ca, O, Mg, Fe, Ti, and Al (Figure S4). The olivine fragments contain an interstitial glassy matrix enriched in Si, Al, and Ca (Figure S5). The glassy regions that make up the bulk of the agglutinitic grain also exhibit dendritic textures that crosscut the grain interior (Figure 4a). These dendritic textures include vein-like, amorphous to weakly crystalline intergrowths with a chromite-like composition and can contain npFe inclusions. EELS analyses of the vesicles in this vein exhibit the presence of the He-K edge ~22 eV (Figure 9). The shape and energy loss position of the He-K edge is variable within the vesicles, and in some cases, two peaks are observed, arising from the two electron transitions 1 s → 2p (~22.4 eV) and 1 s → 3p (~24.6 eV) (Klimenkov et al., 2019). A small feature at ~6 eV is also seen in the EELS spectra, consistent with transitions from the top of the valence band into the $T_{2}g$ and Eg levels of the Ti d orbitals in a nearly octahedral potential, as described for other Ti-bearing oxides by Launay et al. (2004). The shape and position of this feature also match reference EELS spectra of ilmenite collected under comparable conditions, and the presence of Ti in the vein is independently confirmed by EDS.

TEM imaging shows the presence of small ~3 nm diameter npFe particles that extend to a depth of ~200 nm from the grain surface (Figure 4f,g). Spherical and rounded vesicles are present within the top ~50 nm of the grain and range in sizes from 10 to 50 nm in diameter. Some of the chromite-like veins that appear to intersect the grain surface also contain npFe particles, even at depths below the space-weathered rim (Figures 4f–h and 9). Some veins that intersect the grain surface have a more blob-like texture rather than dendritic and contain vesicles and vesicular npFe particles (vnpFe) up to a depth of ~130 nm (Figures 4h and 9). The vnpFe particles contain a range of morphologies, some being spherical and some appearing to be agglomerations of vnpFe particles (Figures 4i and 9). The vesicles in this vein also contain a range of morphologies with some being rounded and others irregularly shaped (Figures 4i and 9). The vesicles in these nanophase Fe particles contain He, regardless of shape or size (Figure 9).

APT Analyses

In the APT reconstructions, there were no density variations that could represent vesicles in the two agglutinitic nanotips. Instead, these nanotips are dominated by Fe-rich structures, including veins of increased Fe and Ti, decreased Mg concentration, and no detectable Cr, and a microphase Fe particle. Although TEM images of a FIB cross section extracted from the same grain show that there are vesicles present, the vesicle-rich layer across the surface is not continuous, and the two nanotips that we analyzed did not sample these features.

Agglutinitic Tip A contains a Ti-rich structure at the apex that is also enriched in Mg, Si, FeO, and a large microphase Fe particle with a Ti-rich rim in the middle (Figure 5). In our reconstruction of Tip A at the lower left is a delicate structure filamentous in cross section view, black arrows in Figure 5. It is most pronounced in TiO, is also enhanced in Ca, Mg, FeO, and slightly in OH (black arrows in Figure 5). At the base is a Ti-rich vein, which is enriched in O, Mg, Si, OH, and H_2O, like the vein at the apex. But in contrast, this vein is strongly enriched in Al, Ca, and H (Figure 5). Agglutinitic Tip B contains some nanophase Fe particles 3–5 nm in diameter at the top 10 nm of the nanotip (Figure 6), before transitioning into an area that is more homogenous. At the base is a Ti-FeO-rich vein which appears to be

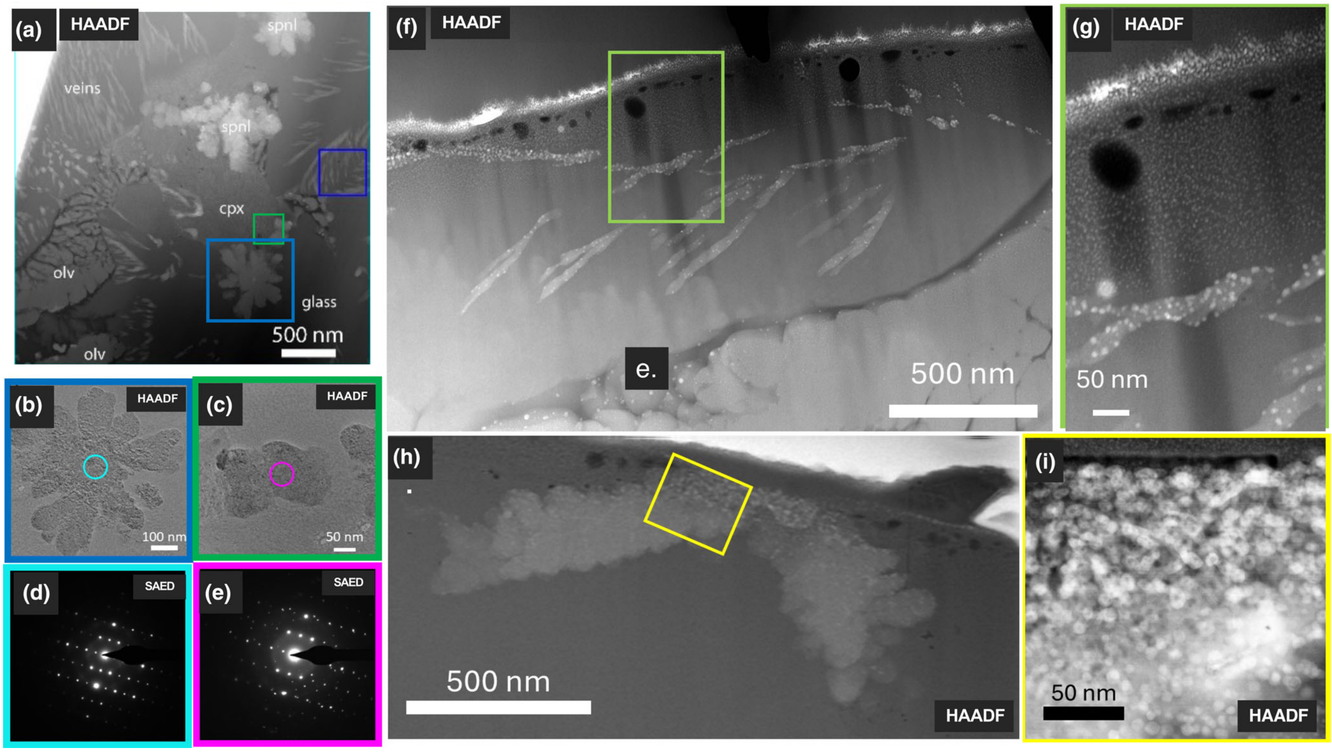

FIGURE 4. TEM images of agglutinitic grain section 2 and included phases within the grain interior. Because vesicles contain less material, the ion beam mills more rapidly through them and leaves the lamella locally thinner below which makes them appear to have shadows. (a) High magnification HAADF image of polyphase agglutinitic grain with multiple included phase such as olivine and clinopyroxene mineral fragments, spinel inclusions, and dendritic veins. (b, c) Crystalline spinel grains present in grain interior. (d, e) SAED patterns of the spinels from (b) and (c), respectively. Both are indexed to spinel. (f) Overview HAADF image of a region in the agglutinitic grain interior. The dark rounded features in a line at the grain surface are vesicles. Dendritic chromite veins containing npFe particles crosscut the grain interior. Deeper into the grain interior is another phase, likely a fragment of a previous grain incorporated into the agglutinitic grain during its formation. (g) Higher magnification HAADF image of an area of the rim from (f). The vesicles at the surface range from ~10 to 50 nm in diameter. Small (~3 nm diameter) npFe particles extend to a depth of ~200 nm from the surface. (h) HAADF image of the grain surface from another FIB section of the agglutinitic grain. Dark circles at the surface are vesicles. A vein with a chromite-like composition and blob-like texture intersects the surface. (i) Higher magnification HAADF image of an area of the surface of the vein from (h). npFe particles are present throughout the vein. npFe particles within the top ~130 nm are vesicular (vnpFe). (Color figure can be viewed at wileyonlinelibrary.com)

deficient in the other elements that occur in the veins of Tip A.

Bladed Agglutinitic Grain

The grain is rounded with linear parallel/subparallel features crossing the surface of the grain (Figure 1c).

TEM Analyses

TEM imaging of a FIB lamella from this grain shows a relatively homogenous glassy matrix containing mineral inclusions that crosscut through the depth of the grain (Figure 7a,b). One of these types of mineral inclusions has an angular, bladed morphology, and EDS analyses are consistent with an ilmenite-like composition. The other type of mineral inclusion has a framboidal texture, and EDS analyses are consistent with an olivine-like composition. The surface of the grain exhibits evidence of space weathering, with variable signatures present in the glassy material, in the areas where ilmenite blades intersect the surface (Figure 7c), and where the framboidal olivine intersects the surface (Figure 7e). The glassy region shows npFe particles ~3 nm in diameter extending ~40 nm from the surface (Figure 7c,f). Some regions of the glassy rim also exhibit irregularly shaped regions that appear bright in BF TEM imaging (Figure 7d). These may represent an interconnected vesicle-like texture. BF-TEM imaging and EDS analyses show an overlying layer at the uppermost surface of the grain enriched in Fe. This Fe correlates to a thin layer of npFe particles at the surface, underlain by a region enriched in Si and O and depleted in other elements (Figure S6). Directly below the Si + O rich layer is another thin zone exhibiting enrichment in Fe due to the

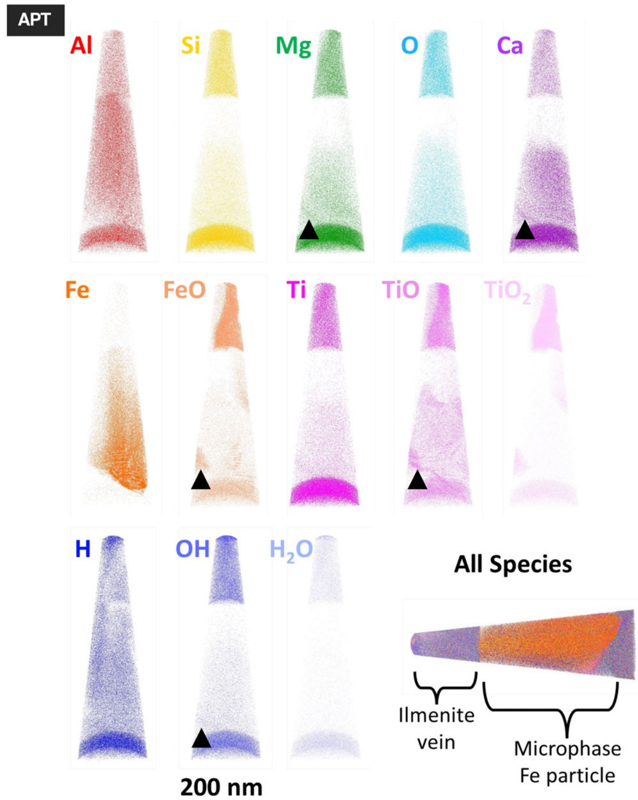

FIGURE 5. APT reconstructions of polyphase agglutinitic grain Tip A: The 2-D projections of 3-D data. Here each major species is shown individually, and then plotted together as "all species." This tip contains a Ti-rich, ilmenite-like vein in the top third, and then is dominated by a large microphase Fe particle in the bottom half. The microphase Fe particle is bordered by a Ti-rich rim. The black arrows indicate a structure filamentous in cross section that is enriched in TiO, Mg, Ca, FeO, and slightly in OH. (Color figure can be viewed at wileyonlinelibrary.com)

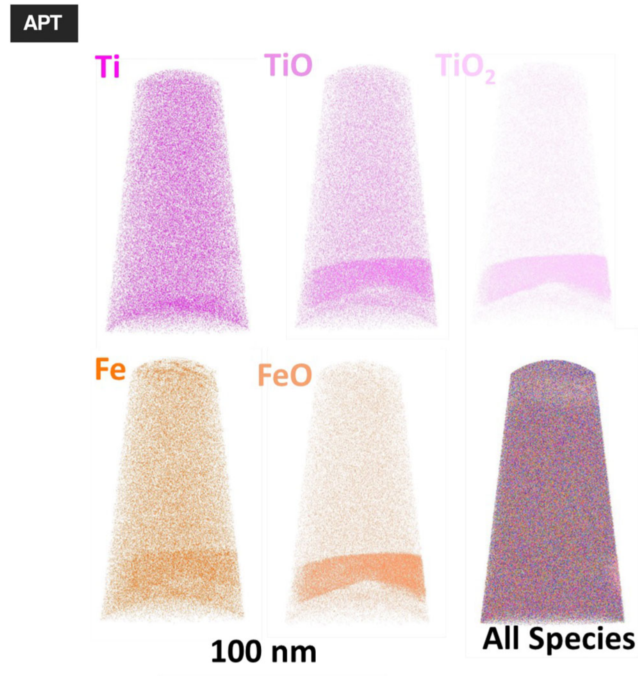

FIGURE 6. APT reconstructions of polyphase agglutinitic grain Tip B: Reconstructions here are 2-D projections of 3-D data. Here Fe- and Ti-bearing species are shown individually, as well as a reconstruction with all major species. Discrete npFe particles are observed at the nanotip apex, and a Fe-enriched vein-like feature occurs near the base. (Color figure can be viewed at wileyonlinelibrary.com)

presence of more npFe particles. There is some enrichment of O away from the surface extending deeper into the grain. Si concentration with depth is variable due to the presence of what may be vesicles, with Si concentration being lower in these areas. The abundances of Ca, Mg, Al, and Ti are generally constant with depth from the surface.

The ilmenite blades that intersect the upper surface of the grain contain elongated, linear vesicles that appear to be positioned parallel to the sides of the ilmenite grain, suggesting a preferred crystallographic orientation (Figure 7c,f). These vesicles extend to ~100 nm deep into the grain from the surface. EELS spectral imaging shows that the elongated vesicles are He-bearing due to the presence of the He-K edge ~22 eV. One ilmenite blade that reaches the grain surface contains a layer of npFe particles and rounded vesicles ~20 nm thick (Figure 7f). The npFe particles in this layer are larger than those in the neighboring glassy material. Additionally, the vesicles in this layer are rounded unlike the elongated vesicles deeper in the ilmenite grain, and are larger than the vesicles present in the neighboring glassy matrix. EELS spectra of the ilmenite have peaks at ~6, 12, 14, 37, and 48 eV associated with TiO_2 (Bosman et al., 2006; Burgess & Stroud, 2018a; Launay et al., 2004). EELS spectra collected from regions of the ilmenite within the space-weathered rim have a broader plasmon peak and broader peaks associated with TiO_2 relative to spectra collected of the bladed ilmenite deeper in the grain.

APT Analyses

A total of five nanotips were prepared from a lamella milled out of the bladed agglutinitic grain, but four of the nanotips fractured at the Pt cap/grain interface. Due to the circumstances of the other four nanotip failures, the remaining Pt on the fifth nanotip was milled away, and because of this, the uppermost 10–20 nm of the surface may be missing. However, there is a small amount of Pt at the apex of the nanotip, present due to implantation during deposition of the protective cap, and therefore perhaps only part of an irregular top ~5 nm of the grain surface is not sampled.

The major elements present this nanotip are Ca, Al, Si, and O, representing a plagioclase-like composition

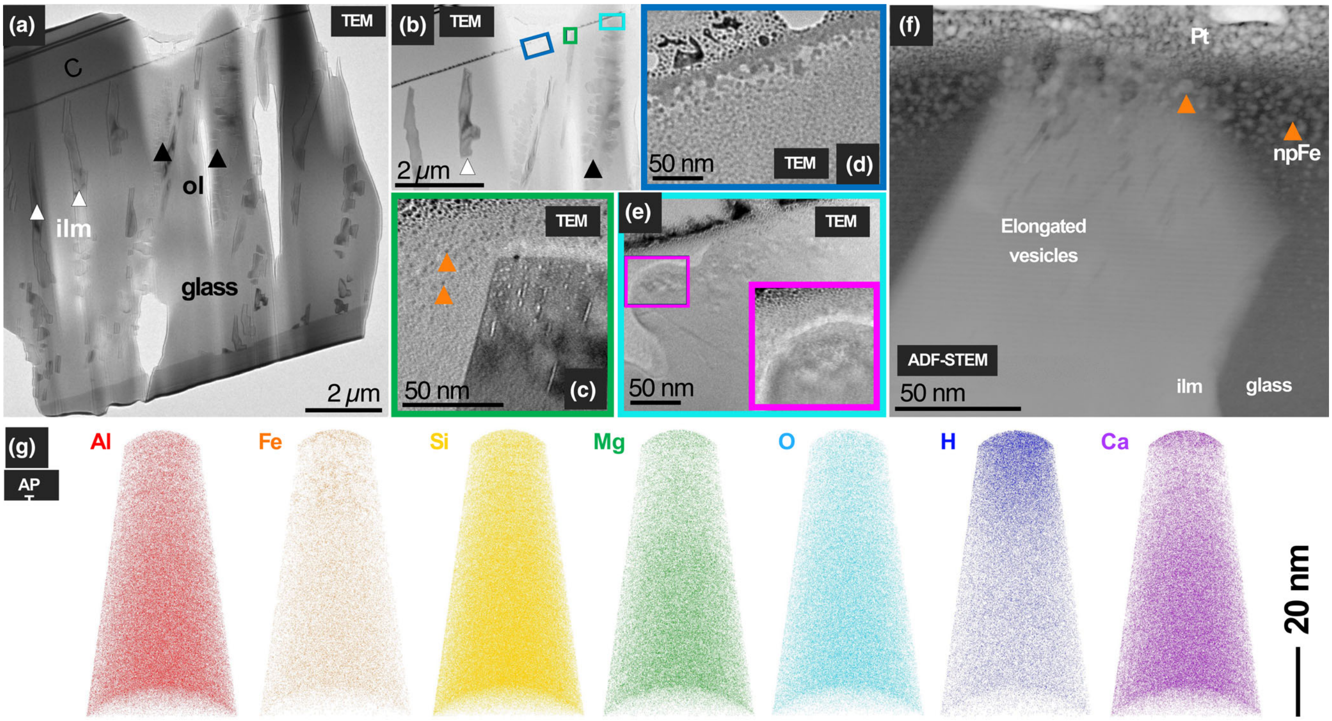

FIGURE 7. Transmission electron microscopy (TEM) images and APT reconstructions of bladed agglutinitic grain from Apollo 79221. (a) Overview image of TEM section. Bladed ilmenite (ilm, white arrows) and framboidal olivine (ol, black arrows) inclusions can be observed cross-cutting through the depth of the grain. (b) Higher magnification TEM image of the space-weathered rim showing locations of areas c–e. (c) TEM image of bladed ilmenite near the surface of the grain intersecting the space weathering rim. npFe particles are present in the glassy region to a depth of ~40 nm (orange arrows). Elongated vesicles are present in the ilmenite blade. (d) TEM image of surface of a glassy region of the grain. Irregularly shaped, bright regions are present below a dark overlying layer. The bright regions may be interconnected vesicle-like structures. (e) TEM image of region of the grain where the framboidal olivine intersects the grain surface. The olivine appears to have an altered texture typical of solar wind irradiation. Some vesicle-like structures may also be present in the upper surface of the olivine. (f) Annular dark field STEM image of bladed ilmenite inclusion intersecting the surface of the agglutinitic grain. The ilmenite contains large npFe particles (white dots) and rounded vesicles at the surface. Elongated vesicles extend deeper into the grain. The glassy region also contains npFe particles up to ~40 nm deep from the surface. Small, rounded vesicles may also be present in this region of the glassy rim as well. (g) APT reconstructions of the bladed agglutinitic grain; 2-D projections of major species. This nanotip sampled the glassy material, and contains npFe particles up to ~20 nm deep. (Color figure can be viewed at wileyonlinelibrary.com)

(Figure 7g). Elements that are present at lower abundances include Mg and Fe. The Fe is distributed heterogeneously, forming clusters of increased concentration (Figure 7g), but not as pure Fe-bearing particles, as these clusters contain other major elements (i.e., Si, O, Mg) present in the mineral, though other elements do not cluster in these locations and therefore do not represent vesicles. We observe concentrations increasing with depth in Al, Mg, and Ca and an opposite trend with H.

Ilmenite

SEM imaging shows that this grain has conchoidal fractures, with some surfaces exhibiting blistering. A few pancake-shaped melt splashes are also present (Figure 1d).

TEM Analyses

High-angle annular dark-field imaging (HAADF) imaging shows that, like the olivine grain, ilmenite has fewer inclusions than the agglutinitic grains (Figure 8a). BF TEM and HAADF STEM imaging of the surface of the ilmenite FIB section shows the presence of a region starting at the grain surface and extending ~50–60 nm deep, containing abundant vesicles and npFe particles (Figure 8b,c). Vesicles in this region are variable in size, though typically ~5 nm in diameter, with some extending up to ~20 nm in diameter, and a few sparse even larger vesicles up to ~100 nm in diameter. The largest vesicles are typically lens-shaped, whereas smaller vesicles in this region are typically rounded and nearly circular. Some smaller vesicles are irregularly shaped and may be interconnected (Figure 8b). The npFe particles in this region are typically ~5 nm in diameter. Below this layer

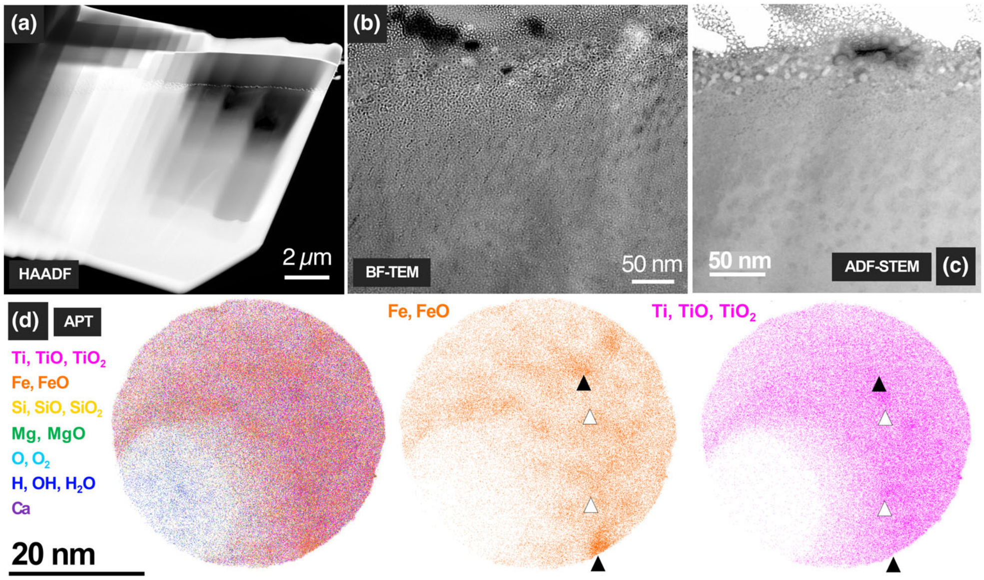

FIGURE 8. Transmission electron microscopy (TEM) images and APT reconstructions of ilmenite grain from Apollo 79221. (a) Overview HAADF image of FIB section of the ilmenite. (b) Overfocused bright-field TEM images of grain surface showing the features of a solar wind-damaged rim. The rim contains rounded and irregularly shaped vesicles as well as npFe particles in the upper surface and small vesicles extended deeper into the grain. (c) Annular dark field STEM image of grain surface. npFe particles are more clearly observed in upper surface. Small vesicles extend deeper into the grain. (d) APT reconstructions of ilmenite, slice looking down the *z*-axis. The vesicle is apparent in the bottom-left quadrant of the top-down projections, as well as clustering in Fe and Ti. The black arrows show Fe clusters with no enhancement in Ti. The white arrows point to Ti clusters that are depleted in Fe. (Color figure can be viewed at wileyonlinelibrary.com)

of vesicles and npFe, even smaller vesicles ~1–3 nm in diameter extend to a depth of ~150 nm from the surface (Figure 8b,c). BF and HAADF STEM images also show that diffraction contrast extends ~200 nm deep from the surface (Figure 8c). This contrast appears to be homogenous toward the surface but gets laterally discontinuous at greater depths into the grain. BF TEM imaging of this region shows that this ~200 nm thick layer appears to be containing dislocation loops (Figure 8b). EDS analyses of the space weathered rim show that the rim is compositionally similar to the grain interior (Figure S7). Within the space weathered rim, the O is depleted toward the surface, with some relative enrichment where Fe is depleted. Ti appears to be anticorrelated with Fe with depth, likely due to the presence of npFe particles observed in this region. The Ti profile is also slightly enriched in a region of O depletion just below the area of Fe depletion. The Mg depth profile is largely consistent in the rim compared to the grain interior, but also appears to have a slight anticorrelation with the Fe profile to a lesser degree than that seen for the Ti profile.

APT Analyses

A total of five nanotips were prepared from a lamella lifted out of the grain that was identified as ilmenite by TEM. Only one nanotip returned data from the target material, and only sampled a few nm in depth. Despite this small data set, there are still features of interest captured. The major elements present in this sample are Fe, Ti, and O with some Mg (bulk ~2.6 at%) and homogenous distribution of Si. Both Ti and Fe are distributed heterogeneously, with the Fe forming clusters 3–5 nm in diameter that likely represent nanophase Fe particles with no measurable enhancement in other elements. We also observe Ti clusters in the same size range which are depleted in Fe (Figure 8d). We observed a large void space (vesicle) measuring about 20 nm across, which contains H and H-bearing molecular species (Figure 8d), and potentially a small amount of ^{4}He. The majority of gaseous content of vesicles is usually lost during APT, but in the mass spectrum of a small sub-volume around the point where the vesicle opened during field-evaporation, there are 5 ± 2 counts at 4 Da. In the bulk of the nanotip, the counts at 4 Da in a sampling volume with the same size range from 0 to 3 atoms.

DISCUSSION

The atom probe nanotips present a large range of composition and structures, even though they are only separated by 1 μm on the grain's surface, consistent with what was observed in the submature lunar soil described in Greer et al. (2020). The heterogeneous distribution of the microstructural and chemical features at the nano- and microscale highlights the complexity of space weathering.

Vesicles

In artificially irradiated materials, He-bearing vesicles form after He atoms in vacancies or interstitials reach a saturation point to form a nucleus, and can grow after continued implantation of He, the introduction of defects, merging with other vesicles, or by coarsening of He bubbles also known as Ostwald ripening (Trinkaus, 1983). Coordinated TEM/APT studies of He-irradiated steels show that the number of vesicles is in part controlled by the amount of He implanted (Li et al., 2014; Lu et al., 2014). Li et al. (2014) also investigated the effect of temperature on He retention, finding that after heat treatment, He concentration decreased and bubble size increased. As impacts from micrometeorites can cause temperatures that vaporize and melt the target rock (Badyukov, 2020; Morgan et al., 1989; Sorokin et al., 2020), some of the vesicles in these lunar samples may have grown to their large size because of this heating.

Measuring He in vesicles in space-weathered samples using APT remains a challenge. As a He-bearing vesicle is exposed to the vacuum during field evaporation, most He atoms in the vesicle escape before they can be ionized (e.g., Li et al., 2014), even at the cryogenic temperatures of 30 to 40 K used in this study. Aside from the detection of He, closed vesiculated textures in space-weathered samples have nonideal geometries. The topography of the nanotip is not an ideal hemisphere due to the presence of these vesicles, which may change the local electric field in ways that lead to nanotip failure. Vesicles that are open to the nanotip's surface and not fully infilled with capping Pt can introduce an instability that leads to nanotip failure during analysis.

The irregular, non-hemispherical shape of a nanotip apex with voids alters the local field evaporation pattern and, consequently, the flight path of the field-evaporated ions. This deviation leads to geometric distortion effects in the reconstructed tomographic data. The distortion occurs because the reconstruction algorithm in IVAS/AP Suite 6 assumes that each detected ion originates from a hemispherically shaped sample surface. For small voids, the ion trajectories around the void curve inward and this region can appear as a high-density region (Wang et al., 2020) in a reconstruction. A similar effect has also been observed for nanoscale fluid inclusions in geologic samples (Dubosq et al., 2021; Taylor et al., 2022). In the samples studied here, smaller vesicles (~1 to 5 nm in diameter) manifest themselves as clusters with a higher atomic density, while larger ones appear as almost empty spaces, with both observed to have higher concentrations of H, OH, and H_2O relative to surrounding rim material (Kling et al., 2025). The larger void spaces (~10 to 50 nm in diameter) can have more complex structures, but it is possible that this is true for the smaller vesicles as well but that this is not resolved in the reconstruction. These vesicle-rich samples are too heterogeneous to use isodensity surfaces to meaningfully locate vesicles simply as regions of lower or higher density in the reconstruction. The complex network of vesicles and defects that are filled with implanted solar wind may not be fully resolvable with APT; as these features change the field-evaporation pattern in the tip (and therefore the flight path of the evaporated ion), and the exact location of some of the ions is not preserved. Changes in the size of these features will result in both areas of increased and decreased density and are difficult to correlate with a single structure. Despite these reconstruction challenges, the coordinated TEM/EELS and APT analysis of aliquots from the same grains is mutually validating. APT identifies H^+, OH^+, and H_2O^+ ions directly from their mass-to-charge ratios, providing an independent line of evidence that low-loss EELS features in the EG energy region can be attributed to water rather than to defects or impurity states, which can produce comparable features particularly in amorphous phases. The H, OH, and H_2O results obtained from these same nanotips, including their spatial association with vesicles, are reported in Kling et al. (2025).

Olivine

Both TEM and APT analyses show the presence of large, rounded vesicles, small, rounded vesicles, and elongated defect structures. The largest rounded vesicles in the olivine are observed in the upper ~30–50 nm of the grain rim while the smaller, rounded vesicles are observed to extend from the surface through the depth of the rim. The elongated defect structures begin below the region of the large, rounded vesicles and extend through the depth of the solar wind-damaged rim. The elongated structures seen in the TEM and with APT in Tip E (Figure 2) are more irregular than the planar defects observed in ilmenite by Burgess and Stroud (2018a), but comparable to those seen in experimentally irradiated ceramic (Zinkle, 2012), olivine (Chrbolková et al., 2022; Laczniak et al., 2024; Zeng et al., 2025), and oxides (Chaves et al., 2023; Igami et al., 2021) which were also wavy and generally parallel to the exposed surface. Zinkle (2012) found that these structures were not associated with a crystallographic orientation and suggested that their orientation was associated with substantial stresses related to the irradiation and implantation. Our observation of the topmost region of the solar wind-damaged rim containing larger, rounded vesicles overlying a region of the rim containing smaller, rounded vesicles and the elongated defect structures is remarkably consistent with the observations of experimentally irradiated olivine (Zeng et al., 2025). Zeng et al. (2025) define these elongated defects as "fractures" and, like Zinkle (2012), attribute their formation to the buildup of localized stress in regions of high defect density. The formation of these fractures may be the result of the merging of vesicles (Zeng et al., 2025) but may also serve as precursors to vesicles and represent the early stages of vesicle formation (Laczniak et al., 2024; Zinkle, 2012).

The presence of all these vesicular structures that can form due to prolonged irradiation and high degrees of radiation damage is consistent with the observed SEP track density corresponding to the expected exposure of a mature soil. These observations are compatible with the trend observed by Keller et al. (2021).

Polyphase Agglutinitic Grain

EELS analyses of the vesicles and the vnpFe particles in the glass phase and the Ti-rich vein in the agglutinitic grain show that they are He-bearing due to the presence of the He-K edge (Figure 9). This He-K edge observed in the vnpFe particles is shifted to higher energies $\sim$24 eV instead of the typical energies $\sim$22 eV, similar to previous observations of He trapped within vnpFe particles (Cymes et al., 2024). The plasmon peak observed within vesicles is broader and shifted to lower energies relative to that observed in the vein material itself, similar to the trend observed in olivine. This is indicative of the lower density of electronic states present in vesicles compared to surrounding matrix material. This observation may be analogous to the lower atomic density in some vesicles relative to surrounding matrix material observed in the APT data of other tips. We note that the absence of vesicles in the APT reconstructions of the polyphase agglutinate tips is itself informative. Given that each nanotip samples a volume only $\sim$100 nm in diameter, and that the vesicle-rich layer is evidently not continuous at this scale, it is likely that these specific tip locations intersected non-vesiculated material. Rather than contradicting the TEM evidence for vesiculation, this observation reinforces the extreme small-scale variability within a single agglutinate grain and underscores the importance of complementing APT with techniques that probe larger volumes.

Bladed Agglutinitic Grain

Unlike in the other grains investigated, vesicles are not a major component of the space weathered surface of the bladed agglutinitic grain glass phase and are only present in areas where the ilmenite blades and framboidal olivine intersect the space weathered region. Planar defects, similar to those seen in Christoffersen et al. (1996) and Burgess and Stroud (2018a), are present within the ilmenite blades included in the plagioclase-like matrix. These defects contain He and are oriented parallel to the ilmenite grain, not perpendicular to the surface of the agglutinitic grain. As this likely follows along a crystallographic plane, it demonstrates how the structure of the crystal influences the formation of these vesicle-like spaces in ilmenite as opposed to the direction of the solar wind. In steel, interfaces between nanoclusters or precipitates are preferred sites for trapping He (Lu et al., 2014). We do not see an increase in the number of vesicles along the edges of the ilmenite blades in contact with the surrounding matrix in the bladed agglutinitic grain, and the defects seem to be more concentrated in the middle of the vein (Figure 7f). The larger, rounded vesicles seen at the top of the ilmenite blade that intersects the grain surface (Figure 7f) may have different morphologies compared to the planar vesicles present in the ilmenite deeper from the surface because of a greater degree of damage in this region, similar to the presence of large, rounded vesicles limited to the upper surface in the olivine we study here (Figure 2) and the experimentally irradiated olivines from Zeng et al. (2025). Alternatively, the large, rounded vesicles at the surface may have grown and become rounded due to elevated heating, such as from a nearby micrometeoroid impact event (Thompson et al., 2017).

Ilmenite

The vesicle in submature ilmenite reported in Greer et al. (2020) is similar in size ($\sim 8 \times 14$ nm) to the vesicle in mature ilmenite shown in Figure 8d ($\sim 11 \times 16$ nm), as reconstructed from APT data. The TEM analysis likewise shows the presence of vesicles of similar scale (Figure 8bc). This sample also included a possible He signal. The burst at the top of the vesicle included an increased detection of H_2, H_3, and ^{4}He (5 ± 2, 1σ, above background; ^{3}He is too low in abundance to be detected here and has an isobaric overlap with H_3). To estimate the expected He amount, we applied the He concentrations for analysis of individual ilmenite grains of sub-mature lunar soil sample 71501 reported by Benkert et al. (1993) to a volume equivalent to that of the observed vesicle. We use the total fusion values for ^{4}He to estimate the minimum concentration of solar wind ^{4}He in ilmenite. We find that, as with the vesicle in submature ilmenite, the vesicle analyzed here contains at least three orders of magnitude fewer He atoms than predicted from bulk concentrations. Although the detected amount of

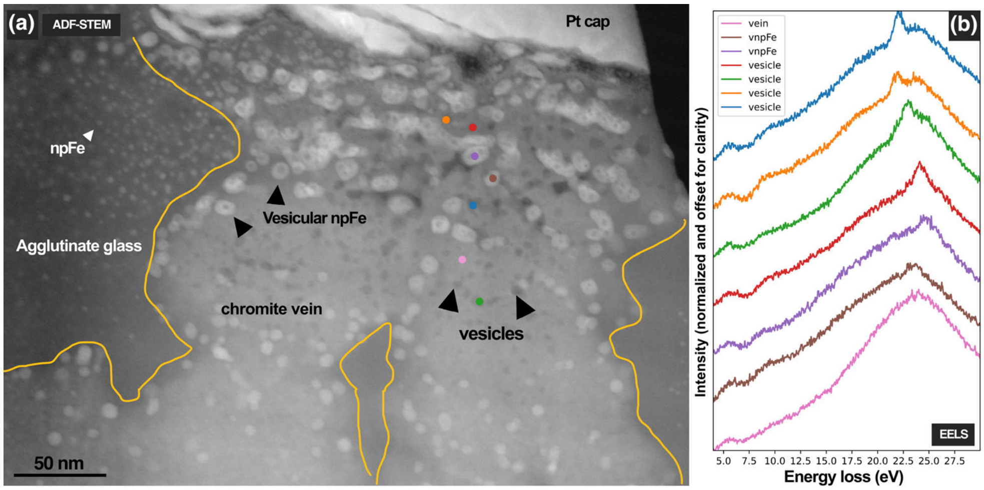

FIGURE 9. Electron energy loss spectroscopy (EELS) spectra from space weathered rim of chromite vein within polyphase agglutinitic grain. (a) Annular dark field (ADF) image of a chromite vein that intersects the surface of the agglutinitic grain. Nanophase Fe particles are present in the glass material and in the vein. Vesicles and vesicular npFe are present in the vein to a depth of ~130 nm. (b) EELS spectra collected from various areas in the vein. EELS spectra collected from vesicles (blue, orange, green, and red) contain the He-K edge with variable energy position and shape. Spectra collected from within vnpFe (lavender, brown) also display the He-K edge with an energy position generally shifted to higher values than in the vesicles. The pink spectrum collected from the vein material does not contain the He-K edge. (Color figure can be viewed at wileyonlinelibrary.com)

He is significantly less than the estimated He content from whole grain analyses of other grains from this soil sample, the ^{4}He peak in the mass spectrum is above the background and above the ^{4}He signal anywhere else in the sample. In this sample, we measure only 0–2 counts of ^{4}He in a volume of identical geometry as the vesicle at random locations in the bulk material outside the vesicle which can be compared to five counts of ^{4}He at the apex of the vesicle with increased H detection. Even this increased concentration requires He loss, likely during the opening and degassing of the vesicle as the top of the nanotip was eroded during analysis. Li et al. (2014) observed interstitial He in a nanostructured ferritic steel alloy (14YWT), but noted that He in vesicles would have been lost to vacuum, and in these lunar samples, if interstitial He is present, it is too low in concentration to be detected in the bulk sample. Similarly, interstitial He is in too low concentration in the rim material outside vesicles to be detected by EELS analyses.

Direct comparison with the samples analyzed in Greer et al. (2020) is difficult: although ilmenite was included in the mature samples that were analyzed so that they could be compared to the submature soil, the mature ilmenite nanotips did not capture a full profile of space weathering products. The mature ilmenite nanotip (Tip C) with the highest counts sampled less than 5 nm depth before it fractured. It is likely that the other mature ilmenite nanotips fractured due to the increased concentration of vesicles relative to the submature sample, which made the nanotips mechanically unstable.

Nanophase Fe

Olivine

In the olivine grain, nanophase Fe is present but limited in abundance. TEM identifies ~3 nm npFe particles within the solar wind-damaged rim (Figure 2c), whereas APT tips generally do not show discrete npFe (Figure 2d,e). In Tip C, Fe-rich clusters correspond to vesicles or voids rather than metallic particles, consistent with the complex vesicular and defect structures documented in TEM (Figures 2b,c) and with their influence on APT field-evaporation behavior.

The small size and low abundance of npFe relative to other studies likely reflect the grain's Mg-rich composition (Fo93), which restricts available Fe for reduction, and the nature of its space weathering history. The surface exposure age (~4.6 ± 0.4 Myr; Kling et al., 2025) and absence of melt features indicate irradiation-dominated weathering rather than repeated high-temperature micrometeoroid impacts that promote npFe coarsening (Thompson et al., 2017). Analyses of space-weathered lunar samples returned by the Chang'e-5 mission suggest that small npFe particles (<5 nm) are formed solely by solar wind irradiation, whereas larger npFe particles form due to contributions from micrometeoroid impacts (Shen et al., 2024). Experimental data also show that abundant npFe forms in fayalitic but not forsteritic olivine under elevated temperatures at ~90°C (Zhang et al., 2025). Stochastic impact processes may still contribute (Basu et al., 1996), but overall the

TEM, EELS, and APT results point to extensive irradiation damage, vesiculation, and volatile implantation with only modest thermal processing and correspondingly limited npFe formation.

Polyphase Agglutinitic Grain

In the polyphase agglutinitic sample, the presence of Fe particles is not limited to the surface of the grains and can be present quite deep into the sample, primarily in the ilmenite veins (Figure 4f). While Fe particles near the surface are a consequence of space weathering, the deeper particles—particularly those confined to ilmenite veins (Figure 4f,g)—are unlikely to be weathering products. A Fe-rich vein of this type is also captured in Tip A by APT (Figure 5) and likely formed as a result of partitioning between immiscible melts during cooling (e.g., Yan et al., 2024). The npFe particles in veins at the surface are larger than those in the agglutinitic grain matrix (Figure 9), either due to this different formation mechanism, because of particle agglomeration, or a combination of both. The effects of space weathering in this sample are observed to manifest as deep as the vesiculated particles are present (~100 nm below the surface).

This vesiculated nanophase Fe was not sampled APT due to the limited volume of the nanotips. Although there are some Fe clusters at the apex of the reconstruction of Tip B (only present in the top ~10 nm: Figure 6), we do not see npFe or vnpFe in the veins in APT. It is unlikely that APT would be able to resolve these vesicles, if they are present, due to the change in the local field evaporation pattern (Wang et al., 2020). The nonspherical morphology of some of the vnpFe particles in the vein has also been observed in lunar agglutinates and has been attributed to the agglomeration of adjacent particles (Cymes et al., 2024). However, the particles observed here appear to represent different stages of agglomeration than those previously observed (Cymes et al., 2024), as some of the structures in these samples are quite complex (Figure 9).

Bladed Agglutinitic Grain

The combined TEM, STEM, and APT observations indicate that the bladed agglutinitic grain preserves a complex space weathering signature involving both melt-derived glass and modified mineral inclusions. The presence of $npFe^0$ to depths of ~40 nm in the glassy rim (Figure 7c,f), together with vesicle networks and vesicle clusters, is consistent with micrometeorite-impact melting and vapor-deposition processes rather than solar wind sputtering alone. The APT results from Tip E further corroborate the shallow distribution of $npFe^0$ within the glassy material (Figure 7g).

The ilmenite blades also show clear evidence of participation in melt-reduction processes. Large $npFe^0$ grains at the ilmenite surface and elongated vesicles extending into the ilmenite along crystallographic orientations (Figure 7c,f) indicate thermal modification and volatile release within the inclusions during agglutinitic grain formation. These textures demonstrate that ilmenite was not preserved as an unweathered exsolution product but experienced melt–vapor interaction and Fe reduction during impact processing.

The framboidal olivine intersecting the surface exhibits an altered texture consistent with solar wind irradiation (Figure 7e), suggesting that some components of the precursor grain retained irradiation features through agglutinitic grain formation. Vesicle-like structures within the shallow olivine rim may record localized heating or devolatilization during the impact event.

The Fe-rich clusters observed in APT Tip E (Figure 7g) are morphologically consistent with early-stage $npFe^0$ grains. Their non-pure Fe composition is likely due to local magnification and trajectory aberrations near the apex of the nanotip rather than true chemical heterogeneity, a well-known analytical artifact in atom probe experiments (e.g., Blavette et al., 2001). These clusters correspond to the large $npFe^0$ particles observed in the ilmenite blades by STEM (Figure 7f).

Together, the features observed in bladed agglutinitic grain (Figure 7f,g) indicate that $npFe^0$ formation, vesiculation, and thermal alteration occurred in both the glassy matrix and the mineral inclusions. The bladed agglutinitic grain exhibits features that may be consistent with micrometeorite-impact melting, vapor deposition, and phase-specific responses to short-duration, high-temperature events.

Ilmenite

Nanophase iron is present in both the mature (this study) and submature (e.g., Greer et al., 2020) ilmenite samples. TEM imaging and EDS mapping (Figure 8; Figure S7) show npFe concentrated in the space-weathered rims and associated with vesicles, consistent with earlier TEM studies of ilmenite rims. The APT data provide a complementary, uniquely 3-D view of these features. In the submature ilmenite, almost all of the Fe sampled by APT is partitioned into npFe particles with Fe-depleted halos (Greer et al., 2020), whereas in the mature ilmenite, the Fe distribution is more heterogeneous at the nanoscale: there are narrow regions adjacent to high-density npFe domains that are depleted in Fe relative to the bulk composition, as well as regions that remain comparatively homogeneous (Figure 10). This ability to resolve Fe-depleted halos immediately

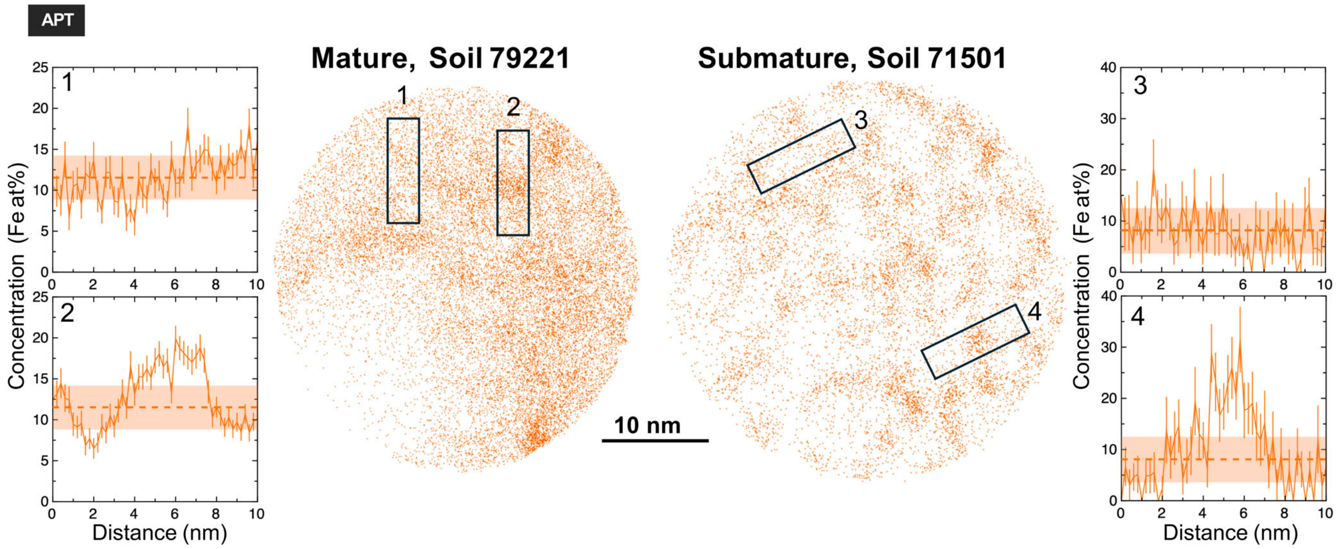

FIGURE 10. APT reconstructions of ilmenite from mature soil Apollo 79221 and submature soil Apollo 71501. Slices of nanotip reconstructions looking down the z-axis of mature and submature ilmenite showing Fe atoms and concentration profiles through selected areas. Each slice is about 3 nm in thickness. While the submature sample shows more distinct clustering than the mature sample, the boundaries of these particles in both nanotips are not as well defined as in TEM imaging. The dashed line shows the average Fe concentration through the sections without clusters (volumes 1 and 3, shaded area is 1σ), which is then superimposed on the sections with clusters (2 and 4) to highlight significant deviations. In section 2, the volume immediately adjacent to the Fe-rich cluster has a Fe concentration below the bulk average. This trend is not pronounced in the particle sampled by section 4. (Color figure can be viewed at wileyonlinelibrary.com)

surrounding npFe particles, and to determine their contrast relative to the bulk composition, is a key advantage of APT for studying space-weathered ilmenite and is difficult to achieve with TEM alone.

It is difficult to define the size of individual npFe particles in the APT reconstruction as the boundaries appear diffuse and adjacent Fe-rich clusters may be interconnected in a sponge-like structure with a high density of Fe-rich particle cores. This may be an intrinsic feature related to the dynamics of their formation. To a certain degree, the interface diffuseness may reflect ion-trajectory aberrations and local magnification effects at phase boundaries between high-field npFe and the surrounding ilmenite, similar to reconstruction artifacts reported in APT studies of nanoscale precipitates and nanoparticles (Lawitzki et al., 2021). Despite these limitations, concentration profiles through selected nanotip segments (Figure 10) consistently show that volumes immediately adjacent to npFe are relatively depleted in Fe, with concentrations below the bulk average, which is not consistent with a typical ion-trajectory aberration effect and supports a scenario in which Fe has migrated from the surrounding ilmenite into the npFe particles.

The trend observed in our APT data is that the submature ilmenite sample exhibits a more complete segregation of Fe into npFe (with little residual Fe in the surrounding matrix), whereas the mature sample retains a mixed character, with both Fe-depleted halos around npFe and regions where Fe remains closer to the bulk value. Simple expectations might predict the opposite behavior, with the more mature sample showing more advanced Fe partitioning into npFe. This apparent reversal could reflect local heterogeneity at the scale of the APT sampling volumes and the limited number of tips analyzed, rather than a global difference in the degree of weathering between the two grains. In the mature sample, vesicle growth may also have influenced Fe redistribution: In Figure 10, the rim at the upper left of the vesicle is slightly enriched in Fe relative to the adjacent matrix, consistent with either displacement of developing npFe toward the vesicle wall during vesicle growth or post-formation migration of Fe toward the vesicle margin.

Within the resolution of our APT data, we do not observe a clear, systematic zonation in Ti or unambiguous stoichiometric partitioning among Ti, TiO, and TiO_2 at the vesicle rim that can be confidently distinguished from analytical scatter. However, the combined TEM and EDS observations (Figure 8; Figure S7) indicate that the space-weathered rims are structurally and chemically complex, and prior studies have reported the formation of distinct Ti-oxide phases in ilmenite rims during space weathering (e.g., Christoffersen et al., 1996; Guo et al., 2024). Taken together with TEM analyses of Apollo 17 and C-E 5 ilmenite (Burgess & Stroud, 2018a; Guo et al., 2024), which show that progressive exposure to space weathering generates damaged rims that evolve into vesicular rims accompanied by increasing npFe formation, our ilmenite data indicate that Fe redistribution into npFe, the development of Fe-depleted halos, and vesicle-related Fe enrichment are all part of the late-stage modification of ilmenite during space weathering. All of our ilmenite samples fall into this vesicular, npFe-rich category.

APT generally provides superior 3-D spatial resolution and higher elemental sensitivity compared to TEM. However, given the complexity of the microstructure, correlating features between APT and TEM can be challenging due to the limited field of view in APT and projection artifacts inherent to 2-D TEM imaging. One possible interpretation is that APT resolves an early stage of npFe formation, in which Fe is modestly enriched in nanoscale clusters forming an interconnected, sponge-like network. With continued irradiation and/or thermal processing, these clusters may coalesce and evolve into more discrete, larger, and more Fe-rich metallic $npFe^0$ particles.

Other Features

Solar Wind Sputtering

Solar wind sputtering and ion-irradiation damage are major drivers of near-surface modification in silicates. Laboratory irradiation studies show that keV H^+ and He^+ implantation causes preferential sputtering, accumulation of collision-cascade damage, and chemical reorganization within the outer tens to hundreds of nanometers (Bradley & Dai, 2009; Chrbolková et al., 2022; Laczniak et al., 2024; Loeffler et al., 2009). The ~120 nm solar wind-damaged rim on our olivine grain lies at the upper end of lunar olivine rims, a thickness that may partially reflect grain orientation relative to the solar wind flux (Zeng et al., 2024). The elongated defects and vesicles in the rim resemble those in experimentally irradiated olivine (Chrbolková et al., 2022; Laczniak et al., 2024; Zeng et al., 2024).

HRTEM, FFT, and EELS analyses (Figures S2 and S3) show progressive amorphization toward the surface, consistent with irradiation-induced breakdown of crystallinity (Bradley et al., 2014; Kushita et al., 1995). Similar amorphous-to-nanocrystalline rims are characteristic of mature lunar regolith olivine (e.g., Keller et al., 2021), and the $\sim 4.6 \pm 0.4$ Myr surface-exposure age of this grain (Kling et al., 2025) is compatible with forming a rim of this thickness.

Although APT cannot directly assess crystallinity, the atomic density decreases slightly near the surface, consistent with increasing structural disorder and complementing the TEM observations. Both TEM-EDS and APT depth profiles (Figure 3) show O depletion in the rim, matching expectations for preferential sputtering (Loeffler et al., 2009). Daly et al. (2021) used APT to analyze a space-weathered Itokawa olivine grain, and their Supporting Data S1 ROI profiles reveal reduced oxygen concentrations in the outer rim relative to the grain interior. This independent APT observation supports the interpretation that solar wind processing can generate O-depleted near-surface regions in olivine.

The Mg-Si zoning observed as layered enrichments and depletions in TEM-EDS (Figure 3) resembles patterns seen in irradiated olivine and phyllosilicates (Laczniak et al., 2024) and in space-weathered Bennu samples (Keller et al., 2025). In contrast, APT does not resolve discrete Mg-Si layers; instead, it shows small-amplitude Mg and Si fluctuations within the outer ~50–80 nm. These variations are consistent with chemical redistribution but fall below the spatial contrast needed to identify distinct lamellae—likely due to the limited sampling volume, trajectory aberrations, and the orientation of the nanotip relative to any planar zoning.

TEM-EDS data for ilmenite (Figure S7) likewise show depletion of O, Mg, Fe, and Ti toward the surface, consistent with sputtering and subsequent diffusion. Similar surface modification has been documented in earlier studies of space-weathered ilmenite. Christoffersen et al. (1996) demonstrated that ion irradiation produces an O- and Fe-depleted, Ti-rich surface layer due to preferential sputtering and reduction, accompanied by nanophase Fe^0 formation. Burgess and Stroud (2018b) likewise observed chemically modified rims and redistribution and reduction of Fe in Apollo 17 ilmenite together with abundant $npFe^0$. Although the mature ilmenite nanotip analyzed here was too short to generate an APT depth profile, submature ilmenite nanotips from Greer et al. (2020) show comparable near-surface O and Fe depletion, paralleling the behavior observed in our olivine grain and reinforcing that ilmenite rims experience similar sputtering-driven chemical modification during space weathering.

Veins in the Agglutinitic Grain

Both TEM and APT analyses of the polyphase agglutinitic grain reveal veins of material within the glassy matrix. TEM-EDS analyses of the Cr-rich dendritic veins show that they are enriched in Fe, Ti, and Cr and depleted in O, Mg, Al, Si, and Ca relative to the surrounding glass (Figure 11), although the exact vein compositions are partly averaged with the adjacent glass through the thickness of the FIB section sampled by the electron beam. The two veins captured in the polyphase agglutinitic grain nanotips exhibit similar chemical trends in APT: Of the major elements present, the veins are

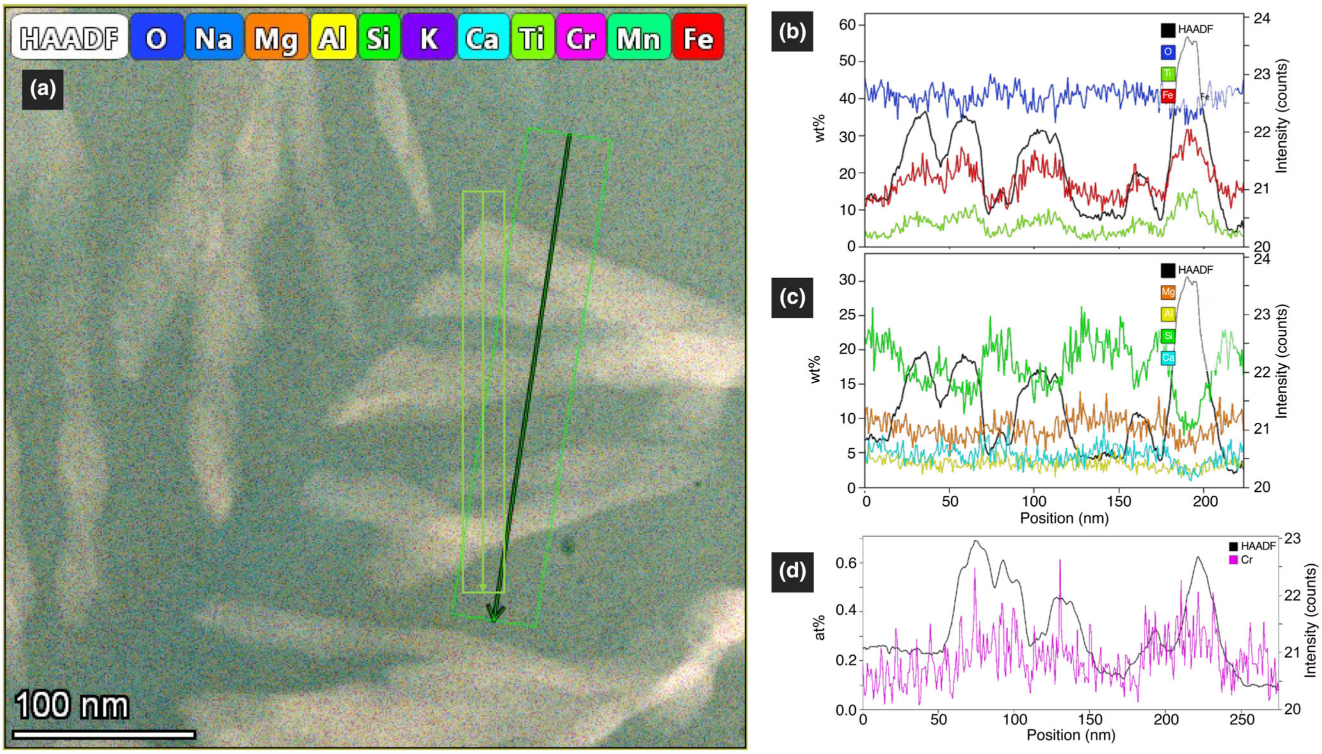

FIGURE 11. EDS maps of chromite-like dendritic veins within glassy interior of agglutinitic grain section 2. (a) HAADF image with EDS map overlays of the veins within the glassy matrix. (b) Linescan data of concentrations of Fe, Ti, and O taken across the veins. The areas of the linescan corresponding to the vein have higher HAADF intensities and are enriched in Fe and Ti and depleted in O relative to the glass. (c) Linescan data of concentrations of Mg, Al, Si, and Ca taken across the veins. The areas of the linescan corresponding to the vein have higher HAADF intensities and are depleted in Mg, Al, Si, and Ca relative to the glass. (d) Linescan data of concentrations of Cr taken across the veins. The areas of the linescan corresponding to the vein have higher HAADF intensities and have slight enrichments in Cr relative to the glass. (Color figure can be viewed at wileyonlinelibrary.com)

enriched in Fe and Ti and depleted in Mg and Si, while O remains approximately constant relative to the surrounding matrix, and no Cr is detected in the APT-sampled volumes (Figure 12). Thus, the veins are not pure ilmenite, but their Fe-Ti-rich, Si-Mg-poor compositions are broadly consistent with a Fe-Ti oxide-dominated melt, chemically related to chromite-like spinel and Fe-Ti-rich domains within the agglutinitic grain. The ~2× higher atomic density in the veins compared to the surrounding glassy matrix (Figure 12) is consistent with a denser Fe-Ti-rich melt that quenched before fully crystallizing, favoring an origin as quench-derived Fe-Ti-oxide dendrites rather than incorporated, preexisting mineral fragments.

The "fuzzy" boundary of the vein in Tip A, which extends over several nanometers (up to ~5 nm; Figure 12), also supports a melt-derived origin. If the veins represented sharp mineral fragments mechanically incorporated into the agglutinitic grain, one would expect more abrupt compositional and density jumps at the vein–matrix interface at APT spatial resolution. Instead, the gradual compositional gradients at the vein margins resemble the diffuse interfaces observed around nanoscale oxide or metal-rich domains in other APT studies, where local magnification effects and short-range diffusion across melt–glass boundaries yield apparent interfaces several nanometers wide. In this context, the diffuse boundary is consistent with a Fe-Ti-rich melt that remained chemically continuous with, and partially intermixed into, the surrounding glass as it quenched.

Glass beads formed through impacts and returned by Chang'e-5 contain similar Fe-Ti-rich veins and dendritic textures (Gu et al., 2023; Pang et al., 2024), and the veins in our sample extend well into the interior of the agglutinitic grain (Figure 4f). Together, these observations indicate that the veins are quench textures formed during agglutinitic grain generation and not features produced by later space weathering processes at the grain surface.

The nanoscale features documented here have implications for remote sensing and in situ resource utilization. Because $npFe^0$ size, abundance, and morphology vary substantially with host mineral within a single mature soil, and because a fraction of the

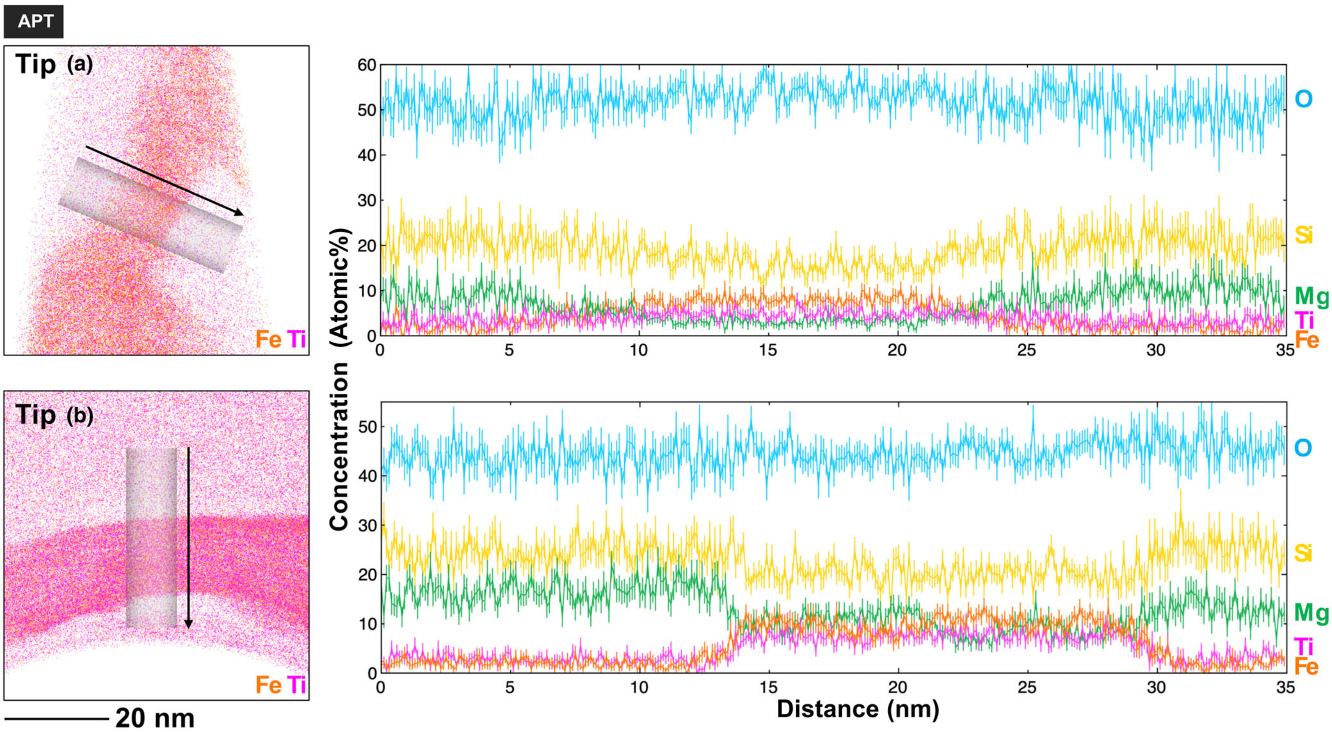

FIGURE 12. APT reconstructions and concentration profiles of veins from polyphase agglutinitic grain nanotips. These reconstruction subsections and concentration profiles were taken from veins at the top of Tip A (Figure 6) and the bottom of Tip B (Figure 7). The nanotip reconstructions plotting Fe and Ti ions show the locations of the cylinders used for the profiles, with the arrow denoting the direction of the profile. Both veins are characterized by increased concentrations of Fe and Ti, with decreased concentrations of Mg and Si, and both are up to 2× as dense as the surrounding material. (Color figure can be viewed at wileyonlinelibrary.com)

agglutinitic $npFe^0$ inventory formed by impact-melting and quenching rather than solar wind reduction, bulk $npFe^0$ parameters used as inputs to spectral-mixing models necessarily average over physically distinct populations. The direct identification of solar wind H, OH, H_2O, and He within sealed vesicles across multiple mineral hosts further indicates that the volatile yield extractable from lunar regolith depends on modal mineralogy and grain-scale rim structure, not bulk maturity alone.

Toward Quantitative APT Analysis of Space-Weathered Lunar Materials

The analytical capabilities of APT are well established for structurally coherent metallic and semiconductor specimens (e.g., Gault et al., 2021). Space-weathered lunar grains pose different challenges: they include electrically insulating materials with strong differences in field-evaporation strength and contain defects such as vesicles that affect field evaporation and ion trajectories. Even though state-of-the art APT instruments with laser-assisted field-evaporation can analyze electrically insulating materials, the standard reconstruction algorithms cannot completely compensate distortions in the atomic reconstructions caused by that complex field-evaporation behavior and thus do not yet yield robust atomic-level quantitative values for space-weathered samples. Specifically, conventional cluster-identification algorithms fail to meaningfully characterize the $npFe^0$ population in our samples: the features are visually unambiguous but diffuse. Therefore, derived number densities and measured feature sizes significantly depend on user-selected parameters. Accordingly, we report the characteristic parameters for $npFe^0$ qualitatively and through concentration profiles rather than attempting to quantify cluster statistics. Absolute concentrations of solar wind-derived volatiles H, OH, H_2O, and He are likewise unreliable near vesicles and phase boundaries, with He most affected because vesicles can release their He budget during field-evaporation as neutral species that are not detected. Field-evaporation can be controlled reasonably well for continuous single-phase glass and olivine, whereas ilmenite, vesicle-rich bladed regions, and Fe-Ti veins are the most difficult for APT analysis. A more quantitative approach is achievable but will require a much larger, methodologically targeted approach and would be the subject of future work.

CONCLUSIONS

This study combines TEM and APT to investigate nanoscale space weathering features in four grains (olivine, ilmenite, and two agglutinitic grains) from mature Apollo 17 soil 79221. By analyzing complementary FIB-extracted sections from the same grains, we reveal the complex structural and chemical evolution of the lunar regolith under solar wind irradiation and micrometeorite bombardment.

All grains exhibit evidence of solar wind damage, vesiculation, and nanophase Fe (npFe) formation, but the extent and morphology of these features vary widely depending on mineralogy and exposure conditions. The olivine shows a ~ 120 nm solar wind-damaged rim containing vesicles and planar defects, whereas the ilmenite has a thinner, intensely vesiculated npFe-rich surface layer with underlying dislocation loops. The agglutinitic grains display dendritic Fe-Ti-Cr-rich veins and vesiculated npFe near their surfaces. Both TEM and APT identify near-surface oxygen depletion, consistent with sputtering effects observed in experimentally irradiated materials. We note that the conclusions of this study are independent of whether individual agglutinic grains are classified as agglutinates or as impact-glass fragments, as both record the space weathering processes that are the focus of this work.

Beyond confirming that nanoscale heterogeneity is a fundamental characteristic of lunar soil and that different minerals within a single mature sample record distinct alteration pathways, our analyses identify several specific advances in understanding lunar space weathering.

First, in mature ilmenite we again resolve, by APT, the Fe-depleted halos immediately adjacent to $npFe^0$ particles that we previously documented with the same technique in submature Apollo 17 ilmenite (Greer et al., 2020), confirming that nanoscale Fe redistribution into $npFe^0$ with associated Fe-depleted halos is a robust feature of ilmenite space weathering and that APT is well suited to resolve these halos against the bulk composition.

Second, in the polyphase agglutinitic grain, we show that Fe-Ti-rich dendritic veins extending through the grain interior are quench textures inherited from impact-melt cooling, not products of in situ space weathering. The vein-hosted $npFe^0$ is therefore not a solar wind exposure indicator and must be distinguished from surface-rim $npFe^0$ when $npFe^0$ inventories are used to estimate maturity or exposure age.

Third, He-bearing planar vesicles in ilmenite blades within the bladed agglutinitic grain appear to align with ilmenite crystal orientation rather than with the geometry of the exposed grain surface, indicating that in mineral inclusions, crystal structure, not solar wind incidence direction, may be the controlling parameter for vesicle morphology and orientation.

Fourth, the Fo93 olivine grain combines a thick (~120 nm) solar wind-damaged rim, abundant vesicles, and clear oxygen depletion with only limited, small $npFe^0$. This decouples rim thickness and exposure age from $npFe^0$ abundance in Mg-rich olivine, in agreement with experimental irradiation studies (Zhang et al., 2025), and indicates that $npFe^0$-based maturity proxies are composition-dependent.

Fifth, our work explores which parameters APT can, and at present cannot, quantify in vesicle-rich, irradiation-damaged grains. Vesicles can appear geometrically distorted in APT reconstructions: small vesicles with diameters in the nanometer range can appear as high-density features in the APT reconstruction; larger vesicles as voids with reduced reconstructed atomic density. Noble gases trapped in vesicles are largely lost during field evaporation in APT. Vesicle networks frequently cause mechanical tip failure, terminating the APT analysis. Consequently, APT-derived counts of vesicles, $npFe^0$, and volatile species in space-weathered grains should be regarded as lower limits. The mutual validation of H, OH, and H_2O detected by EELS and APT (Kling et al., 2025) illustrates the value of the complementary approach utilizing TEM and APT presented here.

Taken together, these nanoscale findings can serve as refined inputs for spectral mixing models of mature lunar regolith and indicate that volatile yields relevant to in situ resource utilization depend on modal mineralogy and grain-scale rim structure, not bulk maturity alone.

Acknowledgments—This work was supported by the NASA Solar System Workings Grant 80NSSC20K0863. AMK was also supported by the NASA FINESST grant 80NSSC23K1368. The authors also acknowledge funding of the Robert A. Pritzker Center by the TAWANI Foundation. We thank the Johnson Space Center Astromaterials Curation Office and the Astromaterials Allocation Review Board for allocation of the lunar samples used in this study. We thank Gerald Olack for maintaining the SEM/FIB Laboratory at the University of Chicago. We acknowledge the use of facilities within the Purdue Electron Microscopy Center (RRID:SCR_022687) at Purdue University. We acknowledge the use of facilities at the Center for Electron Microscopy and Analysis (CEMAS) at The Ohio State University. Atom probe tomography was performed at the Northwestern University Center for Atom-Probe Tomography (NUCAPT, RRID:SCR_017770), acquired and upgraded with equipment grants from the NSF-MRI (DMR-0420532), DURIP-ONR (N00014-0400798, N00014-0610539, N00014-0910781, N00014-1712870, N00014-

2312593), and DURIP-ARO (W911NF2110052) programs. NUCAPT received support from the MRSEC program (NSF DMR-2308691) at the Materials Research Center, the SHyNE Resource (NSF ECCS-2025633), and the Paula M. Trienens Institute for Sustainability and Energy at Northwestern University. LD acknowledges support from UKRI STFC grants (ST/Y004817/1, ST/T002328/1, and ST/W001128/1).

Conflict of Interest Statement—None of the authors have a conflict of interest to disclose.

Data Availability Statement—The APT and TEM data that support the findings of this study are available in a Zenodo repository at https://doi.org/10.5281/zenodo.20090445.

Editorial Handling—Dr. Katherine Joy

REFERENCES

Agrell, S. O., Scoon, J. H., Muir, I. D., Long, J. V. P., McConnell, J. D. C., and Peckett, A. 1970. Mineralogy and Petrology of Some Lunar Samples. *Science* 167: 583–86.

Badyukov, D. D. 2020. Micrometeoroids: The Flux on the Moon and a Source of Volatiles. *Solar System Research* 54: 263–274.

Basu, A., McKay, D. S., Morris, R. V., and Wentworth, S. J. 1996. Anatomy of Individual Agglutinates from a Lunar Highland Soil. *Meteoritics & Planetary Science* 31: 777–782.

Benkert, J.-P., Baur, H., Signer, P., and Wieler, R. 1993. He, Ne, and Ar from the Solar Wind and Solar Energetic Particles in Lunar Ilmenites and Pyroxenes. *Journal of Geophysical Research: Planets* 98: 13147–62.

Bibring, J.-P., Borg, J., Burlingame, A. L., Langevin, Y., Maurette, M., and Vassent, B. 1975. Solar-Wind and Solar-Flare Maturation of the Lunar Regolith. *Proceedings, 6th Lunar Science Conference*, 3471–93.

Blavette, D., Vurpillot, F., Pareige, P., and Menand, A. 2001. A Model Accounting for Spatial Overlaps in 3D Atom-Probe Microscopy. *Ultramicroscopy* 89: 145–153.

Bosman, M., Watanabe, M., Alexander, D. T. L., and Keast, V. J. 2006. Mapping Chemical and Bonding Information Using Multivariate Analysis of Electron Energy-Loss Spectrum Images. *Ultramicroscopy* 106: 1024–32.

Bradley, J. P., and Dai, Z. R. 2009. Analytical SuperSTEM for Extraterrestrial Materials Research. *Meteoritics & Planetary Science* 44: 1627–42.

Bradley, J. P., Dai, Z. R., Erni, R., Browning, N., Graham, G., Weber, P., Smith, J., et al. 2005. An Astronomical 2175 Å Feature in Interplanetary Dust Particles. *Science* 307: 244–47.

Bradley, J. P., Ishii, H. A., Gillis-Davis, J. J., Ciston, J., Nielsen, M. H., Bechtel, H. A., and Martin, M. C. 2014. Detection of Solar Wind-Produced Water in Irradiated Rims on Silicate Minerals. *Proceedings of the National Academy of Sciences of the United States of America* 111: 1732–35.

Burgess, K. D., and Stroud, R. M. 2018a. Phase-Dependent Space Weathering Effects and Spectroscopic Identification of Retained Helium in a Lunar Soil Grain. *Geochimica et Cosmochimica Acta* 224: 64–79.

Burgess, K. D., and Stroud, R. M. 2018b. Coordinated Nanoscale Compositional and Oxidation State Measurements of Lunar Space-Weathered Material. *Journal of Geophysical Research: Planets* 123: 2022–37.

Chapman, C. R. 1996. S-Type Asteroids, Ordinary Chondrites, and Space Weathering: The Evidence from Galileo's Fly-Bys of Gaspra and Ida. *Meteoritics & Planetary Science* 31: 699–725.

Chaves, L. C., Thompson, M. S., Loeffler, M. J., Dukes, C. A., Szabo, P. S., and Horgan, B. H. N. 2023. Evaluating the Effects of Space Weathering on Magnetite on Airless Planetary Bodies. *Icarus* 402: 115634.

Chrbolková, K., Halodová, P., Kohout, T., Ďurech, J., Mizohata, K., Malý, P., Dědič, V., Penttilä, A., Trojánek, F., and Jarugula, R. 2022. Sub-Surface Alteration and Related Change in Reflectance Spectra of Space-Weathered Materials. *Astronomy & Astrophysics* 665: A14.

Christoffersen, R., McKay, D. S., and Keller, L. P. 1996. Microstructure, Chemistry, and Origin of Grain Rims on Ilmenite from the Lunar Soil Finest Fraction. *Meteoritics & Planetary Science* 31: 835–848.

Crozaz, G. 1980. Solar Flare and Galactic Cosmic Ray Tracks in Lunar Samples and Meteorites—What they Tell Us about the Ancient Sun. In *The Ancient Sun: Fossil Record in the Earth, Moon and Meteorites*, edited by R. O. Pepin, J. A. Eddy, and R. B. Merrill, 331–346. New York and Oxford: Pergamon Press.

Cymes, B. A., Burgess, K. D., and Stroud, R. M. 2024. Helium Reservoirs in Iron Nanoparticles on the Lunar Surface. *Communications Earth & Environment* 5: 189.

Daly, L., Lee, M. R., Hallis, L. J., Ishii, H. A., Bradley, J. P., Bland, P., Saxey, D. W., et al. 2021. Solar Wind Contributions to Earth's Oceans. *Nature Astronomy* 5: 1275–85.

Davoisne, C., Leroux, H., Frère, M., Gimblot, J., Gengembre, L., Djouadi, Z., Ferreiro, V., d'Hendecourt, L., and Jones, A. 2008. Chemical and Morphological Evolution of a Silicate Surface under Low-Energy Ion Irradiation. *Astronomy & Astrophysics* 482: 541–48.

Denevi, B. W., Noble, S. K., Christoffersen, R., Thompson, M. S., Glotch, T. D., Blewett, D. T., Garrick-Bethell, I., et al. 2023. Space Weathering at the Moon. *Reviews in Mineralogy and Geochemistry* 89: 611–650.

Dran, J. C., Durrieu, L., Jouret, C., and Maurette, M. 1970. Habit and Texture Studies of Lunar and Meteoritic Materials with a 1 MeV Electron Microscope. *Earth and Planetary Science Letters* 9: 391–400.

Dubosq, R., Rogowitz, A., Schneider, D. A., Schweinar, K., and Gault, B. 2021. Fluid Inclusion Induced Hardening: Nanoscale Evidence from Naturally Deformed Pyrite. *Contributions to Mineralogy and Petrology* 176: 15.

Dukes, C. A., Baragiola, R. A., and McFadden, L. A. 1999. Surface Modification of Olivine by H+ and He+ Bombardment. *Journal of Geophysical Research: Planets* 104: 1865–72.

Erni, R., Browning, N. D., Dai, Z. R., and Bradley, J. P. 2005. Analysis of Extraterrestrial Particles Using Monochromated Electron Energy-Loss Spectroscopy. *Micron* 36: 369–379.

Fegley, B., and Swindle, T. D. 1993. Lunar volatiles: implications for lunar resource utilization. In *Resources of Near-Earth Space*, edited by J. Lewis, M. S. Matthews, and M. L. Guerrieri, 367–426. Tucson: University of Arizona Press.

Gault, B., Chiaramonti, A., Cojocaru-Mirédin, O., Stender, P., Dubosq, R., Freysoldt, C., Makineni, S. K., Li, T., Moody, M., and Cairney, J. M. 2021. Atom Probe Tomography. *Nature Reviews Methods Primers* 1: 51.

Gosling, J. T. 2014. The Solar Wind. In *Encyclopedia of the Solar System*, edited by T. Spohn, D. Breuer, and T. V. Johnson, 3rd ed., 261–279. Amsterdam: Elsevier.

Greer, J., Rout, S. S., Isheim, D., Seidman, D. N., Wieler, R., and Heck, P. R. 2020. Atom Probe Tomography of Space-Weathered Lunar Ilmenite Grain Surfaces. *Meteoritics & Planetary Science* 55: 426–440.

Grün, E., Horányi, M., and Sternovsky, Z. 2011. The Lunar Dust Environment. *Planetary and Space Science* 59: 1672–80.

Gu, L., Lin, Y., Chen, Y., Tang, X., Hu, S., Mao, H., Xu, Y., and Li, J. 2023. Measurement of Ferric Iron in Chang'e-5 Impact Glass Beads. *Earth, Planets and Space* 75: 151.

Guo, Z., Li, Y., Wen, Y., Tai, K., Li, X., Liu, J., and Ouyang, Z. 2022. Nanophase Iron Particles Derived from Fayalitic Olivine Decomposition in Chang'e-5 Lunar Soil: Implications for Thermal Effects during Impacts. *Geophysical Research Letters* 49: e2021GL097323.

Guo, Z., Zhang, M., Jia, B., Li, Y., Fa, W., Pang, Y., Zhu, C., et al. 2024. Space-Weathered Rims on Lunar Ilmenite as an Indicator for Relative Exposure Ages of Regolith. *Communications Earth & Environment* 5: 426.

Hapke, B. 2001. Space Weathering from Mercury to the Asteroid Belt. *Journal of Geophysical Research: Planets* 106: 10039–73.

Housley, R. M., Grant, R. W., and Paton, N. E. 1973. Origin and Characteristics of Excess Fe Metal in Lunar Glass-Welded Aggregates. *Proceedings, 4th Lunar Science Conference*, 2737–49.

Igami, Y., Muto, S., Takigawa, A., Ohtsuka, M., Miyake, A., Suzuki, K., Yasuda, K., and Tsuchiyama, A. 2021. Structural and Chemical Modifications of Oxides and OH Generation by Space Weathering: Electron Microscopic/Spectroscopic Study of Hydrogen-Ion-Irradiated Al_2O_3. *Geochimica et Cosmochimica Acta* 315: 61–72.

Keller, L. P., Berger, E. L., Zhang, S., and Christoffersen, R. 2021. Solar Energetic Particle Tracks in Lunar Samples: A Transmission Electron Microscope Calibration and Implications for Lunar Space Weathering. *Meteoritics & Planetary Science* 56: 1685–1707.

Keller, L. P., and McKay, D. S. 1993. Discovery of Vapor Deposits in the Lunar Regolith. *Science* 261: 1305–7.

Keller, L. P., and McKay, D. S. 1997. The Nature and Origin of Rims on Lunar Soil Grains. *Geochimica et Cosmochimica Acta* 61: 2331–41.

Keller, L. P., Thompson, M. S., Seifert, L. B., Melendez, L. E., Thomas-Keprta, K. L., Le, L., Snead, C. J., et al. 2025. Space Weathering Effects in Bennu Asteroid Samples. *Nature Geoscience* 18: 825–831.

Keller, L. P., Wentworth, S. J., and McKay, D. S. 1998. Space Weathering: Reflectance Spectroscopy and TEM Analysis of Individual Lunar Soil Grains. *29th Lunar and Planetary Science Conference*, abstract #1762.

Keller, L. P., Wentworth, S. J., McKay, D. S., Taylor, L. A., Pieters, C., and Morris, R. V. 1999. Space Weathering in the Fine Size Fractions of Lunar Soils: Soil Maturity Effects. In *New Views of the Moon 2: Understanding the Moon through the Integration of Diverse Datasets*, edited by C. R. Neal, L. R. Gaddis, B. L. Jolliff, S. J. Lawrence, S. J. Mackwell, C. K. Shearer, and S. N. Valencia, 32. Chantilly, Virginia: Mineralogical Society of America and Geochemical Society.

Klimenkov, M., Vladimirov, P., Hoffmann, J., Zimber, N., Möslang, A., and Kuksenko, V. 2019. First Simultaneous Detection of Helium and Tritium inside Bubbles in Beryllium. *Micron* 127: 102754.

Kling, A. M., Greer, J., Thompson, M. S., Heck, P. R., Isheim, D., and Seidman, D. N. 2025. Nanoscale Reservoirs Store Solar Wind-Derived Water on the Lunar Surface. *Earth and Planetary Science Letters* 651: 119178.

Kuhlman, K. R., Sridharan, K., and Kvit, A. 2015. Atom Probe Tomography of Hydrogen-Implanted Olivine: Correlating Nanoscale Chemistry with Infrared Spectral Changes. *Planetary and Space Science* 115: 110–17.

Kushita, K. N., Hojou, K., and Furuno, S. 1995. Electron Energy-Loss Spectroscopy Study of Amorphization Process of Graphite Bombarded with Hydrogen Ions and Energetic Electrons at Low Temperatures. *Microscopy* 44: 456–461.

Laczniak, D. L., Thompson, M. S., Christoffersen, R., Dukes, C. A., Morris, R. V., and Keller, L. P. 2021. Characterizing the Spectral, Microstructural, and Chemical Effects of Solar Wind Irradiation on the Murchison Carbonaceous Chondrite through Coordinated Analyses. *Icarus* 364: 114479.

Laczniak, D. L., Thompson, M. S., Christoffersen, R., Dukes, C. A., Morris, R. V., and Keller, L. P. 2024. Investigating the Role of Incident Ion Flux in Solar Wind Space Weathering of Carbon-Rich Asteroidal Regolith Via H+ and He+ Irradiation of the Murchison Meteorite. *Icarus* 410: 115883.

Launay, M., Boucher, F., and Moreau, P. 2004. Evidence of a Rutile-Phase Characteristic Peak in Low-Energy Loss Spectra. *Physical Review B* 69: 035101.

Lawitzki, R., Stender, P., and Schmitz, G. 2021. Compensating Local Magnifications in Atom Probe Tomography for Accurate Analysis of Nano-Sized Precipitates. *Microscopy and Microanalysis* 27: 499–510.

Lewis, J., Isheim, D., Jolliff, B., Seidman, D., Ogliore, R., and Gillis-Davis, J. 2020. Nanometer-Scale Analysis of Space-Weathered Lunar Regolith by Atom Probe Tomography. *Microscopy and Microanalysis* 26: 2584–87.

Leya, I., and Masarik, J. 2009. Cosmogenic Nuclides in Stony Meteorites Revisited. *Meteoritics & Planetary Science* 44: 1061–86.

Li, Q., Parish, C. M., Powers, K. A., and Miller, M. K. 2014. Helium Solubility and Bubble Formation in a Nanostructured Ferritic Alloy. *Journal of Nuclear Materials* 445: 165–174.

Li, Y., Li, X., Wang, S., Li, S., Tang, H., and Coulson, I. M. 2013. Crystal Orientation Results in Different Amorphization of Olivine during Solar Wind Implantation. *Journal of Geophysical Research: Planets* 118: 1974–82.

Lin, J., Zhang, H., Qian, Y., Hu, S., and Li, C. 2025. Differences in Space Weathering between the Near and Far Side of the Moon: Evidence from Chang'e-6 Samples. *National Science Review* 12: nwaf087.

Loeffler, M. J., Dukes, C. A., and Baragiola, R. A. 2009. Irradiation of Olivine by 4 keV He+: Simulation of Space Weathering by the Solar Wind. *Journal of Geophysical Research: Planets* 114: E03003.

Lu, C., Lu, Z., Xie, R., Liu, C., and Wang, L. 2014. Microstructure of a 14Cr-ODS Ferritic Steel before and after Helium Ion Implantation. *Journal of Nuclear Materials* 455: 366–370.

Matsumoto, T., Noguchi, T., Tobimatsu, Y., Harries, D., Langenhorst, F., Miyake, A., and Hidaka, H. 2021. Space Weathering of Iron Sulfides in the Lunar Surface Environment. *Geochimica et Cosmochimica Acta* 299: 69–84.

Matsumoto, T., Tsuchiyama, A., Miyake, A., Noguchi, T., Nakamura, M., Uesugi, K., Takeuchi, A., Suzuki, Y., and Nakano, T. 2015. Surface and Internal Structures of a Space-Weathered Rim of an Itokawa Regolith Particle. *Icarus* 257: 230–38.

McKay, D. S., Heiken, G., Basu, A., Blanford, G., Simon, S., Reedy, R., French, B. M., and Papike, J. 1991. The Lunar Regolith. In *The Lunar Sourcebook: A User's Guide to the Moon*, edited by G. H. Heiken, D. T. Vaniman, and B. M. French, 285–356. Cambridge: Cambridge University Press.

Meyer, C. 2009. *Lunar Sample Compendium*. Houston, TX: Astromaterials Research & Exploration Science, NASA.

Morgan, T. H., Zook, H. A., and Potter, A. E. 1989. Production of Sodium Vapor from Exposed Regolith in the Inner Solar System. *19th Lunar and Planetary Science Conference*, 297–304.

Morris, R. V. 1978. The Surface Exposure (Maturity) of Lunar Soils—Some Concepts and Is/FeO Compilation. *9th Lunar and Planetary Science Conference*, 2287–97.

Noble, S. K., Pieters, C. M., and Keller, L. P. 2007. An Experimental Approach to Understanding the Optical Effects of Space Weathering. *Icarus* 192: 629–642.

Noguchi, T., Kimura, M., Hashimoto, T., Konno, M., Nakamura, T., Zolensky, M. E., Okazaki, R., et al. 2014. Space-Weathered Rims Found on the Surfaces of the Itokawa Dust Particles. *Meteoritics & Planetary Science* 49: 188–214.

Noguchi, T., Nakamura, T., Kimura, M., Zolensky, M. E., Tanaka, M., Hashimoto, T., Konno, M., et al. 2011. Incipient Space Weathering Observed on the Surface of Itokawa Dust Particles. *Science* 333: 1121–25.

Pang, R., Yang, J., Li, R., Liu, S., Li, Q., Zhu, D., Du, W., and Liu, Y. 2024. Redox Condition Changes Caused by Impacts: Insights from Chang'e-5 Lunar Glass Beads. *Science Bulletin* 69: 1495–1505.

Pieters, C. M., and Noble, S. K. 2016. Space Weathering on Airless Bodies. *Journal of Geophysical Research: Planets* 121: 1865–84.

Pieters, C. M., Taylor, L. A., Noble, S. K., Keller, L. P., Hapke, B., Morris, R. V., Allen, C. C., McKay, D. S., and Wentworth, S. 2000. Space Weathering on Airless Bodies: Resolving a Mystery with Lunar Samples. *Meteoritics & Planetary Science* 35: 1101–7.

Rocca, M. 1995. Low-Energy EELS Investigation of Surface Electronic Excitations on Metals. *Surface Science Reports* 22: 1–71.

Serventi, G., and Carli, C. 2017. The Role of Very Fine Particle Sizes in the Reflectance Spectroscopy of Plagioclase-Bearing Mixtures: New Understanding for the Interpretation of the Finest Sizes of the Lunar Regolith. *Icarus* 293: 157–171.

Shen, L., Zhao, R., Chang, C., Yu, J., Xiao, D., Bai, H., Zou, Z., Yang, M., and Wang, W. 2024. Separate Effects of Irradiation and Impacts on Lunar Metallic Iron Formation Observed in Chang'e-5 Samples. *Nature Astronomy* 8: 1110–18.

Sorokin, E. G., Yakovlev, O. I., Slyuta, E. N., Gerasimov, M. V., Zaitsev, M. A., Shcherbakov, V. D., Ryazantsev, K. M., and Krasheninnikov, S. P. 2020. Experimental Modeling of a Micrometeorite Impact on the Moon. *Geochemistry International* 58: 113–127.

Taylor, L. A., Pieters, C. M., Keller, L. P., Morris, R. V., and McKay, D. S. 2001. Lunar Mare Soils: Space Weathering and the Major Effects of Surface-Correlated Nanophase Fe. *Journal of Geophysical Research: Planets* 106: 27985–99.

Taylor, L. A., Pieters, C. M., Keller, L. P., Morris, R. V., McKay, D. S., Patchen, A., and Wentworth, S. 2001. The Effects of Space Weathering on Apollo 17 Mare Soils: Petrographic and Chemical Characterization. *Meteoritics & Planetary Science* 36: 285–299.

Taylor, S. D., Gregory, D. D., Perea, D. E., Kovarik, L., Cliff, J. B., and Lyons, T. W. 2022. Pushing the Limits: Resolving Paleoseawater Signatures in Nanoscale Fluid Inclusions by Atom Probe Tomography. *Earth and Planetary Science Letters* 599: 117859.

Thompson, M. S., Zega, T. J., Becerra, P., Keane, J. T., and Byrne, S. 2016. The Oxidation State of Nanophase Fe Particles in Lunar Soil: Implications for Space Weathering. *Meteoritics & Planetary Science* 51: 1082–95.

Thompson, M. S., Zega, T. J., and Howe, J. Y. 2017. In Situ Experimental Formation and Growth of Fe Nanoparticles and Vesicles in Lunar Soil. *Meteoritics & Planetary Science* 52: 413–427.

Trinkaus, H. 1983. Energetics and Formation Kinetics of Helium Bubbles in Metals. *Radiation Effects* 78: 189–211.

Wang, X., Hatzoglou, C., Sneed, B., Fan, Z., Guo, W., Jin, K., Chen, D., et al. 2020. Interpreting Nanovoids in Atom Probe Tomography Data for Accurate Local Compositional Measurements. *Nature Communications* 11: 1022.

Weinberg, Z. A., Rubloff, G. W., and Bassous, E. 1979. Transmission, Photoconductivity, and the Experimental Band Gap of Thermally Grown SiO_2 Films. *Physical Review B* 19: 3107–17.

Wurz, P., Fatemi, S., Galli, A., Halekas, J., Harada, Y., Jäggi, N., Jasinski, J., et al. 2022. Particles and Photons as Drivers for Particle Release from the Surfaces of the Moon and Mercury. *Space Science Reviews* 218: 10.

Yan, P., Xiao, Z., Wu, Y., Wu, Y., Pan, Q., Luo, F., and Xu, R. 2024. Submicroscopic Iron-Rich Grains throughout Impact Glasses in Chang'e-5 Regolith. *Icarus* 410: 115920.

Zeng, X., Jin, Z., Bose, M., Hervig, R., and Long, T. 2025. Effects of Crystal Orientation and Temperature on Space Irradiation of Silicates. *The Astrophysical Journal* 991: 159.

Zeng, X., Wu, Y., Yu, W., Mo, B., Wen, Y., Zhao, X., Li, X., Zhang, X., and Liu, J. 2024. Unusual Ti Minerals on the Moon Produced by Space Weathering. *Nature Astronomy* 8: 1–7.

Zhang, T., Tang, H., Li, X., Yu, W., Wen, Y., Zhou, C., Mo, B., and Liu, J. 2025. Formation of np-Fe0 Particles by H+ Irradiation: Insight into Space Weathering on the Moon and Other Airless Bodies. *Astronomy & Astrophysics* 703: 13.

Zhu, C., Góbi, S., Abplanalp, M. J., Frigge, R., Gillis-Davis, J. J., and Kaiser, R. I. 2019. Space Weathering-Induced Formation of Hydrogen Sulfide (H_2S) and Hydrogen Disulfide (H_2S_2) in the Murchison Meteorite. *Journal of Geophysical Research: Planets* 124: 2772–79.

Zinkle, S. J. 2012. Effect of H and He Irradiation on Cavity Formation and Blistering in Ceramics. *Nuclear Instruments and Methods in Physics Research Section B: Beam Interactions with Materials and Atoms* 286: 4–19.

SUPPORTING INFORMATION

Additional supporting information may be found in the online version of this article.

Figure S1. APT time-of-flight mass spectra of the eight nanotips. Peak identifications have been color-coded. The spectra are shown without background correction.

Figure S2. (a) BF-TEM image of solar wind-irradiated rim of olivine overlying grain interior. (b) High-resolution (HRTEM) image of the solar wind irradiated rim. The white line indicates the grain surface. The colored boxes correspond to locations where Fast-Fourier Transform (FFT) analyses were collected. (c–e) FFTs corresponding to the colored boxes in (b). All three FFTs show the nanocrystalline nature of the solar wind-damaged rim via the presence of diffraction spots. The grain shows increasing amorphization toward the surface, as indicated by the loss of discrete diffraction spots and emergence of diffuse rings (c).

Figure S3. Changes to EELS spectra with depth through space-weathered rims. (a) ADF STEM image of the rims of olivine. Markers indicate pixels from which EELS spectra were extracted. (b) Low-loss EELS spectra collected through the depth of the rims of olivine. Going from the grain interior toward the surface, there is a shift in the plasmon peak maximum to lower energy loss as well as a broadening of the plasmon peak, both indicative of changes to the bonding environment induced by solar wind irradiation.

Figure S4. EDS maps of clinopyroxene grain fragment in agglutinitic grain section 2 interior. (a) BF image clinopyroxene grain fragment in agglutinitic grain interior. (b–h) EDS 27 element maps of olivine fragment. Veins enriched in Ti and Fe, are present and of similar 28 compositions to veins elsewhere in the agglutinitic grain glass.

Figure S5. EDS maps of olivine grain fragment in polyphase agglutinitic grain section 2 interior. (a) DF image of olivine grain fragment in agglutinitic grain interior. (b–f) EDS element maps of olivine fragment. Glassy interstitial veins enriched in Si, O, and Al crosscut through the olivine grain, possibly indicative of melting during agglutinitic grain formation.

Figure S6. EDS map and concentration profile of space-weathered glassy region of the bladed agglutinitic grain. The rim contains npFe particles throughout its depth except in a thin layer just below the surface which is enriched in Si and O. Si concentration is variable with depth due to the presence of npFe particles. The concentrations of Ca, Mg, Al, and Ti are somewhat constant with depth from the surface.

Figure S7. Energy dispersive X-ray spectroscopy (EDS) elemental maps and concentration profiles with depth through the space-weathered rim of ilmenite. (a) HAADF image and corresponding elemental maps of Fe, Ti, O, and Mg. The green line and box indicate the region over which the line profile in b is averaged. The dashed white lines indicate approximate areas corresponding to variations in the chemical trends observed in the depth profile. (b) Depth profile of elemental concentrations with depth through the space-weathered rim.